Design of Complementary PCFM Waveform Set for Smearing Spectrum Jamming Suppression in MIMO Radar Systems

XIANGFENG QIU, Graduate Student Member, IEEE
WEIDONG JIANG
XINYU ZHANG
YONGXIANG LIU
National University of Defense Technology (NUDT), Changsha, China

SYMEON CHATZINOTAS, Fellow, IEEE
University of Luxembourg, Luxembourg City, Luxembourg
Kyung Hee University, Yongin-si, South Korea

MARIA SABRINA GRECO, Fellow, IEEE
FULVIO GINI, Fellow, IEEE
University of Pisa, Pisa, Italy

The smeared spectrum (SMSP) jamming technique generates dense comb-shaped false targets at the receiver, making it difficult to detect the target of interest. Waveform design introduces greater flexibility at the transmitter, offering the potential for active antijamming strategies. This article investigates countermeasures to SMSP jamming in multiple-input–multiple-output radar systems by designing phase-coded frequency-modulated (PCFM) waveforms. Moreover, the complementary PCFM waveform design scheme is considered to further expand the design freedom, utilizing the coherence between multiple pulses to achieve improved performance. Specifically, we first formulate the complementary waveform design as a multiobjective optimization problem, by unifing the SMSP jamming levels, the waveform sidelobes, and the waveform orthogonality after the matched filter processing at the receiver into a set of fractional terms. Subsequently, the optimal complementary PCFM waveforms are obtained by employing the iterative algorithm based on the approximated Hessian matrix of the objective functions. Numerical simulations are conducted to demonstrate that the designed complementary PCFM waveforms significantly improve SMSP jamming suppression and enhance target detection performance.

Received 11 December 2024; revised 12 March 2025; accepted 10 April 2025. Date of publication 14 April 2025; date of current version 11 August 2025.

DOI. No. 10.1109/TAES.2025.3560612

Refereeing of this contribution was handled by J. Xu.

The work of X. Qiu was supported in part by the China Scholarship Council, in part by the National Natural Science Foundation of China under Grant 62022091 and Grant 61921001, and in part by the Graduate Innovation Capacity Enhancement Program under Grant ZC41370323108. The work of F. Gini and M.S. Greco was supported in part by the Italian Ministry of Education and Research (MUR) in the framework of the FoReLab project (Departments of Excellence) and in part by the University of Pisa under Grant PRA 2022 91 INTERCONNECT.

Authors' addresses: Xiangfeng Qiu, Weidong Jiang, Xinyu Zhang, and Yongxiang Liu are with the College of Electronic Science and Technology, National University of Defense Technology (NUDT), Changsha 410073, China, E-mail: (qxf1981993100@163.com; jwd2232@vip.163.com; zhangxinyu90111@163.com; bible@sina.com); Symeon Chatzinotas is with SnT, University of Luxembourg, 1855 Luxembourg City, Luxembourg and also with the College of Electronics & Information, Kyung Hee University, Yongin-si 17104, South Korea, E-mail: (maria.greco@unipi.it); Fulvio Gini is with the Department of Information Engineering, University of Pisa, 56122 Pisa, Italy, E-mail: (fulvio.gini@unipi.it). *(Corresponding author: Xiangfeng Qiu.)*

I. INTRODUCTION

A. Background and Motivation

Radar systems have become crucial components in advancing the environmental perception of intelligent vehicle systems [1], [2]. However, the increasing use of onboard radar systems has raised the risk of malicious active electronic jamming, which can obscure genuine targets and severely compromise the reliability of radar-based environmental sensing [3], [4], [5]. This jamming presents a direct and unavoidable threat to the effectiveness of vehicle systems. In response, the emergence of cognitive radar has marked a significant shift in radar antijamming strategies [6], [7], [8]. Traditionally, radar systems employed passive, fixed-mode jamming mitigation techniques at the receiver end. In contrast, cognitive radar enables active jamming suppression at the transmitter level, allowing the system to dynamically adjust its emission parameters in real time to respond to changing environmental conditions [9], [10], [11]. This article focuses on the design of complementary phase-coded frequency-modulated (PCFM) waveforms to effectively mitigate smeared spectrum (SMSP) jamming in multiple-input–multiple-output (MIMO) radar systems [12], [13], [14], thereby enhancing the performance of onboard radar sensors in environments subjected to active jamming.

B. Smeared Spectrum Jamming Countermeasure

The widespread adoption of digital radio frequency memory (DRFM) technology [15], [16] has spurred the development of various jamming techniques and advanced countermeasures. A notable example is the SMSP jamming [17], which represents a form of self-protective deception. This technique involves the creation of tightly packed, spurious signals arranged in a comb-like structure around the target, effectively degrading the radar system's ability to detect the genuine target.

Recent research on SMSP jamming mitigation has largely focused on receiver-side echo processing techniques. These include transform domain filtering [18], [19], signal reconstruction [20], [21], [22], and multichannel

separation methods [23], [24]. Transform domain filtering works by converting the echo signals to a different domain, allowing the separation of target signals through windowing or nulling the jamming main lobe. Signal reconstruction techniques estimate and remove the jamming components by inferring the jamming parameters. Multichannel separation is effective in situations where there are significant angular or polarization differences between the target and jamming signals. However, filtering methods can result in considerable target energy loss, reconstruction approaches are computationally intensive due to the complexity of parameter estimation, and multichannel techniques are limited by the operational conditions of the radar system.

The rapid progress of cognitive radar systems [7] highlights waveform design and coherent signal accumulation [25] as a promising strategy for mitigating SMSP jamming. Research, such as [26] and [27] has explored cognitive waveform design specifically for SMSP scenarios, with an emphasis on reducing auto-correlation sidelobes and minimizing cross-correlation between the SMSP jamming signals and the radar filter. The majorization-minimization (MM) technique [28] is used to simplify and solve the corresponding optimization problem. In addition, the approach in [29] integrates waveform design with sparse decomposition to address the dense false targets caused by SMSP. To further improve jamming suppression, the author in [30] investigated the joint optimization of the transmit waveform and space-time receive filter, to reduce both autocorrelation sidelobe levels and cross-correlation peaks (CCP) of jamming signals. This work introduces an iterative penalty MM method to handle the resulting nonconvex optimization. While these studies show promising results in SMSP jamming suppression, they primarily focus on single-channel radar systems. However, modern vehicle radar systems are predominantly multichannel, and the challenge of applying waveform optimization for jamming mitigation in MIMO radar systems remains an area that requires further investigation.

C. Design of PCFM Waveform

The PCFM waveform is a variant of the continuous phase modulation (CPM) scheme [31], specifically adapted for certain communication systems [32]. It serves as a bridge between mathematically structured phase codes and physically realizable frequency-modulated (FM) waveforms, facilitating the conversion of arbitrary polyphase codes into FM waveforms suitable for high-power radar transmission. More importantly, this approach allows for the direct design of FM waveforms by optimizing the parameterized code structure to meet the desired characteristics of the resulting waveform, thereby integrating the code-to-waveform mapping into the design process [33]. Furthermore, this method enables the inclusion of transmitter-induced distortions—such as those arising from the power amplifier—into the waveform design, mitigating their detrimental effects [33], [34], while also facilitating the coupling of spatial and polarization degrees of freedom with the waveform [35].

Substantial research has been conducted on the design of PCFM waveforms to achieve optimal waveform performance. To reduce the integrated sidelobe level (ISL) of the PCFM waveform, the authors in [33] employed a greedy search strategy to perform a linear search in phase space. To further enhance design efficiency, Mohr et al. [36] proposed an alternative method based on the phase gradient descent algorithm. The authors in [37] explored a design approach for complementary PCFM waveforms that exploits the coherent properties of multiple pulses to achieve a superposition of mainlobe energy and sidelobe energy cancellation, thereby further reducing the ISL. To expand the degrees of freedom in signal processing, the authors of [38], [39], and [40] proposed a joint design approach for both the transmit PCFM waveform and the receive filter. Several studies also focus on achieving specific spectral properties of PCFM waveforms through waveform design techniques, as demonstrated in [41], [42], and [43]. While these efforts successfully optimize waveform performance, they are largely confined to single-channel radar systems. To address this limitation, the authors in [44] extended their investigation to the optimization of PCFM waveforms in a dual-channel system, although practical MIMO systems typically involve many more channels. Despite the extensive development and application of PCFM waveforms, existing research has predominantly concentrated on designing PCFM waveforms with low sidelobes and sparse spectral characteristics. Extending the design of PCFM waveforms to MIMO radar systems, while ensuring robust jamming immunity, remains a novel and underexplored area.

D. Proposed Approach and Main Contributions

In this study, we explore a method for suppressing SMSP jamming in MIMO radar systems by designing the complementary PCFM waveform set, with the goal of improving system performance in SMSP jamming environments. To start, we define a waveform design problem that aims to reduce both the waveform sidelobe levels and the SMSP jamming response level processed by the matched filter (MF) in the receiving end. Furthermore, we ensure that the waveforms maintain orthogonality across different channels to minimize inter-channel interference. To tackle the nonconvex nature of the problem, we further propose an iterative algorithm based on the approximated Hessian of the objective functions to iteratively find the optimal solution. The key contributions of this work are summarized as follows.

1. Waveform Design Problem for SMSP Suppression in MIMO Radar: In contrast to existing methods that focus on mitigating SMSP in single-channel radar systems, this study proposes a novel approach specifically designed for MIMO radar systems. The central focus of the proposed methodology is to establish a multiobjective optimization problem, aiming to minimize the sidelobes realized by the transmit waveform from the same channel, while concurrently minimizing the cross-correlation levels between the

SMSP component and the waveform. To address the challenges of channel interdependence and mutual SMSP jamming minimization, the proposed approach integrates the concept of response minimization for waveform-waveform pairs and waveform-SMSP pairs associated with distinct channels, thereby enhancing the overall system resilience in the jamming environment in the presence of SMSP.

2. Employment of Complementary PCFM Waveforms for Enhanced SMSP Suppression: To ensure the necessary spectral containment and constant amplitude for high-power transmitters, we constrain the waveform transmitted by each channel in the MIMO system to adhere to the PCFM scheme. In addition, due to the inherent advantage of complementary waveform sets in accumulating signal energy and canceling sidelobe levels, we propose the joint configuration of multiple sequentially transmitted pulses on each channel. This approach increases the degrees of freedom available for waveform optimization, thereby improving the design of transmit waveforms that meet the specified performance requirements.

3. Approximated Hessian-Based Algorithm for the Transmit Waveform Design: To address the challenges posed by the nonconvex nature of the transmit waveform optimization problem, we employ an iterative algorithm based on the approximated Hessian matrix of the objective functions to efficiently search for the optimal phase values embedded within the PCFM waveforms. First, we provide a detailed derivation of the gradient corresponding to the waveforms, thereby enabling the application of the proposed optimization algorithm. Next, the computational complexity is assessed by analyzing the dominant computation steps. Numerical simulations are conducted to validate the effectiveness of the proposed algorithm in generating orthogonal PCFM waveforms with favorable auto-correlation, cross-correlation, and SMSP suppression characteristics.

E. Outlines and Notations

The rest of this article is as follows: Section II presents the discrete principles of SMSP jamming and the mathematical foundation for the design of the complementary PCFM waveform set. Section III provides a detailed description of the proposed approximated Hessian-based algorithm. Section IV demonstrates the algorithm's effectiveness in SMSP suppression through the numerical simulations. Finally, Section V concludes this article.

In this article, bold uppercase letters represent matrices, while bold lowercase letters denote vectors. The symbol $(\cdot)^H$ refers to the conjugate transpose, $(\cdot)^*$ represents the complex conjugate, and $(\cdot)^T$ indicates the transpose operation. The function diag$(\cdot)$ creates a diagonal matrix with the entries of a vector along its diagonal. The Hadamard product and modulus are denoted by $\odot$ and $|\cdot|$, respectively. The real and imaginary parts of a complex number are extracted using the functions Re$(\cdot)$ and Im$(\cdot)$, and $\|\cdot\|_p$ represents the l_p norm of a vector. The convolution operation is denoted by $\otimes$, and j denotes the imaginary unit, where $j^2 = -1$. Finally, $\langle\cdot,\cdot\rangle$ represents the inner product operator.

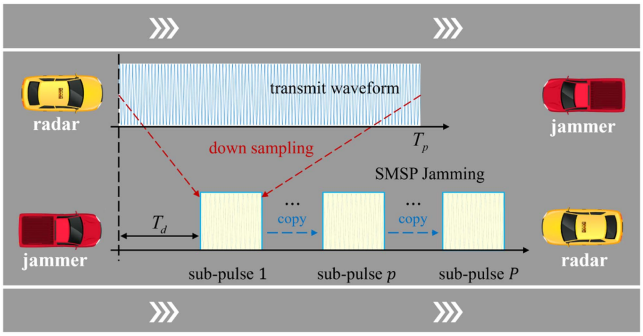

Fig. 1. Illustration of SMSP jamming principle. The yellow vehicle uses an onboard radar system to detect the surrounding environment, while the red vehicle employs its own SMSP jammer to interfere with the radar system, thereby preventing the exposure of its own information. T_p denotes the pulse width of the transmit waveform, T_d denotes the time delay of the SMSP jamming and P is the number of subpulses and the down-sampling rate.

II. PROBLEM FORMULATION

A. Discrete Signal Model of SMSP

The SMSP is a typical form of signal-dependent jamming designed to interfere with pulse-Doppler radar systems. In Fig. 1, we show schematic diagrams of two vehicles, one equipped with a radar system to detect the surrounding environment, and the other using an SMSP jammer to interfere with the radar system. Specifically, the SMSP jammer first down-samples the intercepted radar waveform by a factor of P to extract the jamming subpulse. This subpulse is then repeated P times to form the complete SMSP jamming signal, ensuring that the pulse width remains the same as the original radar pulse. This downsampling approach effectively spreads the spectrum of the jamming signal across the frequency domain, ensuring that it overlaps with the frequency range of the target of interest. Furthermore, by repeating the SMSP component P times, the energy of the jamming signal is amplified while maintaining consistent coverage of the target echo throughout the entire pulse duration. This dual effect of spectral spreading and energy enhancement significantly enhances the effectiveness of the jamming signal. Since the jamming signal is closely related to the radar waveform, it causes the formation of false targets when accumulated coherently at the receiver. Mathematically, the shift matrix used to model the generation of the SMSP jamming signal can be given by

$$\mathbf{J} = [\mathbf{I}_{\text{SMSP}}, \ldots, \mathbf{I}_{\text{SMSP}}]_{L\times L} \tag{1}$$

where $\mathbf{I}_{\text{SMSP}}$ is represented as

$$\mathbf{I}_{\text{SMSP}} = \begin{bmatrix} \overbrace{1\ 0\ \cdots\ 0}^{P} & & \\ & \ddots & \\ & & \overbrace{1\ 0\ \cdots\ 0}^{P} \end{bmatrix}_{\bar{L}\times L} \tag{2}$$

with $\bar{L}$ and L denote the length of subpulses and the total length of the SMSP jamming signal. The relationship $L = P \cdot \bar{L}$ always holds, according to the principle of SMSP jamming. The principle is visually illustrated in Fig. 1.

To address the subsequent complementary PCFM waveform design problem, we describe the method for estimating the shift matrix $\mathbf{J}$. Based on the SMSP jamming mechanism shown in Fig. 1, the matrix $\mathbf{J}$ can be determined by first identifying the downsampling factor P, followed by calculating the sample length of the subpulse, $\bar{L}$. In the field of waveform design, it is commonly assumed that the necessary prior information is acquired through cognitive radar [45]. In practical scenarios, such information can be extracted from the received echoes. For radar systems that employ linear frequency modulation (LFM) waveforms, the key parameters of the SMSP jamming signal can be estimated by applying time-frequency transformation techniques to the received signal [21]. To establish a more generalized approach, we propose a parameter estimation method for SMSP jamming based on a sparse recovery framework. Denoting the transmit waveform with $\boldsymbol{s} \in \mathcal{C}^N$, the radar echoes contaminated by SMSP jamming at the receiver can be expressed as

$$\mathbf{r} = \mathbf{r}_t + \mathbf{J} \cdot \mathbf{s} + \mathbf{n} \tag{3}$$

where $\mathbf{r}_t$ denotes the target echoes, and $\mathbf{n}$ is the noise of the radar system. Thus, the shift matrix $\mathbf{J}$ can be obtained by solving the following problem:

$$\min_{\mathbf{J}} \ \|\mathbf{r} - \mathbf{r}_t - \mathbf{J} \cdot \mathbf{s}\|_2^2 + \sigma \ \|\mathbf{J}\|_1 \tag{4}$$

where the target component can be obtained by the blind source separation method [46], [47], the l_1-norm penalty term $\|\mathbf{J}\|_1$ is employed to constraint the sparsity characteristics of the shift matrix, and σ is the penalty factor. Employing the alternating direction method of multipliers (ADMM) method and the soft-threshold method [48], the above optimization problem can be addressed and the shift matrix $\mathbf{J}$ obtained.

B. Implementation of PCFM Waveform

The waveform design strategy for SMSP suppression outlined here is based on the PCFM implementation framework, which is a radar-optimized variant of CPM originally developed for communications. The authors in [31], [32], [33], and [34] introduced a four-step methodology for deriving a complex baseband PCFM waveform from an N-length column vector $\mathbf{x}$. This procedure is mathematically expressed as

$$\begin{aligned} & s(t; \mathbf{x}) \\ &= \exp\left\{ j \left[\int_0^t g(t) \otimes \left(\sum_{n=1}^{N} x_n \delta\left(t - (n-1) T_{\text{sub}}\right) \right) d\tau \right] \right\} \\ &= \exp\left(j\phi(t; \mathbf{x})\right), \end{aligned} \tag{5}$$

where $T_p = NT_{\text{sub}}$, T_{sub} is the duration of each subpulse, $\delta(t)$ represents the impulse function, and $g(t)$ is a frequency-shaping filter with time support on $[0, T_{\text{sub}}]$, which smooths the discontinuities between phases in the vector $\mathbf{x}$.

By formulating the phase component of the PCFM in this way, it becomes amenable to discretization through sampling the phase function as described in (5). This discretization allows the efficient evaluation of the PCFM waveform using a single matrix-vector multiplication. Thus, the discretized PCFM waveform of length L can be expressed as

$$\mathbf{s} = \exp\left(j\mathbf{G}\mathbf{x}\right) \tag{6}$$

where $\mathbf{G}$ is an $L \times N$ matrix containing the sampled phase function $\phi(t; \mathbf{x})$ [33]. By employing an oversampling strategy with a factor Q as proposed by Jakabosky et al. [49], the relationship $L = Q \times N$ is established. As a result, with careful selection of the parameters in $\mathbf{x}$, it is possible to generate PCFM waveforms that exhibit the desired characteristics.

C. PCFM Waveform Design for SMSP Suppression

Consider an MIMO radar system with M channels, where each channel transmits K pulses during a coherent processing interval (CPI), with each pulse containing L sampling points. It is also important to note that the concept of waveform diversity is applied not only to each channel but also to the different pulses within the CPI.

Let $\mathbf{s}_m^k = \exp(j\mathbf{G}\mathbf{x}_m^k)$ represent the kth transmit pulse from the mth channel of the MIMO radar system, where $\mathbf{x}_m^k = [\mathbf{x}_m^k(1), \ldots, \mathbf{x}_m^k(n), \ldots, \mathbf{x}_m^k(N)]^T$. The matrix form of the desired complementary PCFM waveform can then be formally expressed as

$$\mathbf{S} = \begin{bmatrix} \exp\left(j\mathbf{G}\mathbf{x}_1^1\right) & \cdots & \exp\left(j\mathbf{G}\mathbf{x}_M^1\right) \\ \vdots & \ddots & \vdots \\ \exp\left(j\mathbf{G}\mathbf{x}_1^K\right) & \cdots & \exp\left(j\mathbf{G}\mathbf{x}_M^K\right) \end{bmatrix}_{KN \times M} \tag{7}$$

where each column of $\mathbf{S}$ represents the K pulses transmitted by each channel. Then, the complementary correlation functions among the PCFM waveforms can be given as

$$\mathbf{r}_{m_1,m_2} = \sum_{k=1}^{K} \mathbf{F}^H \left[\left(\mathbf{F}\bar{\mathbf{s}}_{m_1}^k\right) \odot \left(\mathbf{F}\bar{\mathbf{s}}_{m_2}^k\right)^* \right] \tag{8}$$

where $m_1, m_2 = 1, \cdots M$, $\bar{\mathbf{s}}_m^k = [(\mathbf{s}_m^k), \mathbf{0}_{1\times(L-1)}]^T$, $\mathbf{F}$ denotes the fast Fourier transform (FFT) matrix. For $m_1 = m_2$, $\mathbf{r}_{m_1,m_2}$ represents the complementary auto-correlation of waveforms within the same channel, while the others represent the complementary cross-correlation between waveforms from different channels. It is worth noting that (8) performs a complex-valued summation of the correlation values of the K PCFM waveforms within the same CPI. This coherent processing technique can enhance the main lobe while simultaneously reducing the sidelobes by appropriately designing the parameters of the different waveforms. Similarly, the SMSP jamming component associated with the kth PCFM waveform from the mth channel can be

expressed as $\xi_m^k = \mathbf{J}\mathbf{s}_m^k$. Consequently, the complementary correlation functions corresponding to the waveform-SMSP pairs can be expressed as

$$\mathbf{r}_{m_1,m_2}^J = \sum_{k=1}^{K} \mathbf{F}^H \left[\left(\mathbf{F}\bar{\mathbf{s}}_{m_1}^k \right) \odot \left(\mathbf{F}\bar{\xi}_{m_2}^k \right)^* \right] \tag{9}$$

where $m_1, m_2 = 1, \cdots M$, $\bar{\xi}_{m_2}^k$ represents the zero-padded version of $\xi_{m_2}^k$, with a dimension of $(2L-1) \times 1$. As shown in (8), by optimizing the waveform parameters across multiple pulses, the main lobes of these pulses can be constructively superimposed, while their sidelobes can be mutually canceled, leading to enhanced pulse compression (PC) performance. Similarly, through careful optimization of PCFM waveform parameters in (9), the SMSP jamming responses corresponding to different pulses can be mutually canceled, resulting in significantly improved jamming suppression performance. This approach not only leverages the complementary characteristics of multiple waveforms but also achieves a balance between main lobe enhancement and sidelobe/jamming suppression, offering a solution to the challenges posed by coherent jamming.

Before formally introducing the waveform design model, it is essential to clarify the distinction between phase-coded waveforms and PCFM waveforms. In conventional phase-encoded waveform design, the problem is often reduced to the design of the corresponding phase sequence. This simplification is well-founded, as the performance of the waveform is primarily dictated by the properties of the encoding phase sequence. During implementation, the designed phase sequence is modulated to produce the corresponding time-domain waveform. Notably, for a given phase sequence, the peak of its autocorrelation function is a constant value determined solely by the sequence length. In this study, we adopt a different perspective by focusing on the PCFM regime. Within this framework, the main lobe in the PC output exhibits a specific width, which is influenced by the oversampling factor. While the peak response of the main lobe remains determined by the waveform length, the responses at other points within the main lobe are no longer constant. This distinction highlights a key difference in the behavior of PCFM waveforms compared to traditional phase-coded waveforms, providing a foundation for subsequent analysis and design approach. Using the components described above, the multiobjective optimization problem for designing the complementary PCFM waveform set toward SMSP suppression can be formulated in the following four parts.

1) To achieve optimal target detection performance, it is typically required that the transmit waveform exhibits extremely low sidelobe levels after MF processing. Therefore, the waveform design should focus on minimizing the following metric:

$$f_1\left(\mathbf{x}_1^k, \ldots, \mathbf{x}_M^k\right) = \sum_{m=1}^{M} \frac{\left\|\mathbf{r}_{mm} \odot \mathbf{w}_{\mathrm{SL}}\right\|_p^2}{\left\|\mathbf{r}_{mm} \odot \mathbf{w}_{\mathrm{ML}}\right\|_p^2} \tag{10}$$

where $\mathbf{w}_{\mathrm{SL}}$ is designed to select the sidelobe points, with a length of $2L-1$, consisting of ones for all elements except for the central $2Q-1$ elements, which are set to zero. Similarly, $\mathbf{w}_{\mathrm{ML}}$ is designed to select the mainlobe points, with the central $2Q-1$ elements set to one, and the remaining elements set to zero. By defining these two vectors, the 3-dB bandwidth can be controlled using the oversampling factor Q, and a low sidelobe waveform can be obtained by minimizing the function component.

2) To reduce mutual interference among PCFM waveforms from different channels, the overall response values across all range bins after MF processing must be suppressed. Therefore, the following function component needs to be minimized:

$$f_2\left(\mathbf{x}_1^k, \ldots, \mathbf{x}_M^k\right) = \sum_{m_1,m_2=1,m_1\neq m_2}^{M} \frac{\left\|\mathbf{r}_{m_1m_2}\right\|_p^2}{\left\|\mathbf{r}_{m_1m_1} \odot \mathbf{w}_{\mathrm{ML}}\right\|_p^2}, \tag{11}$$

where the numerator represents the total response values of the complementary cross-correlation of PCFM waveforms between different channels, while the denominator represents the mainlobe values of the auto-correlation within a single channel. By minimizing this function component, the ratio of the cross-correlation between channels to the mainlobe of the auto-correlation within a single channel is reduced, thereby achieving the goal of suppressing inter-channel interference.

3) To minimize the overall SMSP jamming energy in each channel after the MF processing at the receiver, it is crucial to minimize the following functional component:

$$f_3\left(\mathbf{x}_1^k, \ldots, \mathbf{x}_M^k\right) = \sum_{m=1}^{M} \frac{\left\|\mathbf{r}_{mm}^J\right\|_p^2}{\left\|\mathbf{r}_{mm} \odot \mathbf{w}_{\mathrm{ML}}\right\|_p^2}. \tag{12}$$

In each term of the summation in (12), the numerator represents the total energy of the SMSP jamming component after the MF processing at the receiver, while the denominator represents the mainlobe energy of the corresponding PCFM waveform. By minimizing this component, the jamming response can be effectively suppressed, achieving the SMSP jamming mitigation.

4) Similar to the function component in (11), we also need to mitigate the mutual interference associated with the waveform-SMSP pairs from distinct channels by minimizing the following subfunction:

$$f_4\left(\mathbf{x}_1^k, \ldots, \mathbf{x}_M^k\right) = \sum_{m_1,m_2=1,m_1\neq m_2}^{M} \frac{\left\|\mathbf{r}_{m_1m_2}^J\right\|_p^2}{\left\|\mathbf{r}_{m_1m_1} \odot \mathbf{w}_{\mathrm{ML}}\right\|_p^2}, \tag{13}$$

where the numerator is the jamming response energy caused by the waveform-SMSP pairs from different

channels, while the denominator corresponds to the mainlobe energy of the waveform.

Employing the function components (10)–(13), the final complementary PCFM waveform design problem toward SMSP suppression can be expressed as

$$f\left(\mathbf{x}_1^k, \ldots, \mathbf{x}_M^k\right) = \sum_{i=1}^{4} \alpha_i \cdot f_i\left(\mathbf{x}_1^k, \ldots, \mathbf{x}_M^k\right) \tag{14}$$

where α_i represents the weight assigned to $f_i(\mathbf{x}_1^k, \ldots, \mathbf{x}_M^k)$. In practical applications, it is essential to allocate weights to the individual subobjective functions based on specific priorities and operational requirements. To ensure uniform weighting across all subfunctions, the weights are set to $\alpha_i = 1$.

Based on the model described in (14), the proposed method achieves SMSP suppression by disrupting the phase coherence between the jamming component and the waveform. This is realized through the codesign of parameters in the complementary PCFM waveform. By reducing the response magnitude of the SMSP component after PC, the method effectively suppresses SMSP. Although the modeling process assumes that the target and the jammer are colocated, the proposed method is also applicable to scenarios where the target and the jammer are spatially separated, as the delay of the jamming component does not affect the amplitude response of the PC process. This ensures the method robustness in various spatial configurations.

It is important to note that SMSP jammers typically do not incorporate Doppler modulation into the intercepted waveforms. As a result, our approach focuses on accumulating multiple pulses to achieve the desired waveform performance in the fast-time dimension. Consequently, the objective function established in this study does not account for the Doppler dimension, and this is a commonly used strategy in the field of complementary waveform design [50]. However, if the application of the designed complementary waveforms in the Doppler domain becomes necessary, a viable solution is to treat the multiple complementary pulses as a single, extended pulse. This extended pulse can then be transmitted repeatedly in the slow-time dimension at a specified pulse repetition interval. At the receiver, the echoes can be processed in the slow-time dimension to extract the desired information. This approach ensures flexibility in adapting the designed waveforms to scenarios requiring Doppler domain utilization.

It is also worthwhile to stress that while the individual terms involving the p-norms of the signal vectors $\mathbf{r}_{m_1,m_2}$ and $\mathbf{r}^J_{m_1,m_2}$, weighted by the sidelobe window $\mathbf{w}_{\mathrm{SL}}$ and mainlobe window $\mathbf{w}_{\mathrm{ML}}$, are convex for $p \geq 1$, the overall convexity of the objective function is influenced by the nonlinear behavior introduced by the complex exponential function $\exp(j\mathbf{G}\mathbf{x}_m^k)$. This nonlinearity, stemming from the periodic nature of the exponential term, creates interactions between the optimization variables that prevent the function from being convex. Specifically, the complex exponential introduces periodicity, which can result in multiple local minima and, therefore, a nonconvex optimization landscape. As a result, despite the convexity of individual components, the presence of nonlinear exponential terms makes the objective function nonconvex, leading to a complex optimization problem with the potential for multiple local minima and no guarantee of a globally optimal solution.

III. PROPOSED METHOD

A. Gradient-Based Algorithm

The optimization problem formulated in (14) is inherently nonconvex, posing substantial challenges due to the absence of guaranteed global optimal solutions. In the context of waveform design, nonconvex optimization models typically lack analytically tractable solutions, necessitating the use of iterative algorithmic frameworks to approximate suboptimal results. Various optimization strategies, such as the MM and ADMM approaches, are employed to address this issue. These methods adapt to the specific structure of the objective function and the constraints imposed on the optimization variables, enabling the derivation of feasible and near-optimal solutions through iterative refinement. However, in many engineering applications, achieving a local optimal solution is often sufficient. In [36], the conjugate gradient descent (CGD) method is employed to solve a similar single-channel nondeterministic polynomial (NP) problem, suggesting that it may be effective for our problem as well. Thus, it is reasonable to extend the gradient-based algorithm from [36] to find a locally optimal solution for the multiple-channel waveform optimization problem within the jamming suppression framework. However, since the CGD algorithm relies solely on the first-order gradient, it is prone to slow convergence and may yield suboptimal solutions. To address these limitations, we employ a second-order optimization algorithm, which incorporates approximated Hessian information of the objective function to enhance convergence speed and improve the quality of the solution.

By stacking the phase vectors $\mathbf{x}_1^k, \ldots, \mathbf{x}_M^k$ as follows:

$$\mathbf{X} = \begin{bmatrix} \mathbf{x}_1^1 & \cdots & \mathbf{x}_M^1 \\ \vdots & \ddots & \vdots \\ \mathbf{x}_1^K & \cdots & \mathbf{x}_M^K \end{bmatrix}_{KN \times M} \tag{15}$$

we can express the update of the phase matrix $\mathbf{X}$ in a more compact form within the gradient-based framework [51]

$$\mathbf{X}_{t+1} = \mathbf{X}_t + \beta_{t+1} \cdot \mathbf{D}_{t+1} \tag{16}$$

where $\mathbf{X}_{t+1}$ is the phase matrix at the $(t+1)$th iteration, β_{t+1} is the step size, and $\mathbf{D}_{t+1}$ represents the descent direction at the same iteration. During the CGD algorithm, the Armijo condition also referred to as the first Wolfe condition [6], is commonly employed in gradient descent algorithms to determine the optimal step size. Moreover, its descent direction relies solely on first-order gradient information to determine the descent direction. This limitation often leads to slow convergence and suboptimal solutions, especially in complex optimization problems.

Algorithm 1: Two-Loop Recursion for L-BFGS.

Input: $\{\Delta\mathbf{X}_i, \Delta\mathbf{Y}_i\}$, and $\rho_i = 1/\langle\Delta\mathbf{X}_i, \Delta\mathbf{Y}_i\rangle$ for all $i \in t-z+1, \cdots, t$, the gradient $\nabla f(\mathbf{X}_{t+1})$;
Output: the descent direction $\mathbf{D}_{t+1}$;

$\mathbf{R} = \nabla f(\mathbf{X}_{t+1})$;
for $i = t, \cdots, t-z+1$ **do**
  $\gamma_i = \rho_i \langle\Delta\mathbf{X}_i, \mathbf{R}\rangle$;
  $\mathbf{R} = \mathbf{R} - \gamma_i \Delta\mathbf{Y}_i$;
end
$\mathbf{R} = \mathbf{H}_t^0 \mathbf{R}$;
for $i = t-z+1, \cdots, t$ **do**
  $\eta_i = \rho_i \langle\Delta\mathbf{Y}_i, \mathbf{R}\rangle$;
  $\mathbf{R} = \mathbf{R} + (\gamma_i - \eta_i)\Delta\mathbf{X}_i$;
end
compute the descent direction $\mathbf{D}_{t+1} = -\mathbf{R}$;

Algorithm 2: Complementary PCFM Waveform Design Method Toward SMSP Suppression.

Input: M, N, K, J, L, Q, T, p
Output: designed complementary PCFM waveform.

Initialize $\mathbf{G}$, $\mathbf{X}^{(0)}$, $\Delta\mathbf{X}^{(0)}$, $\Delta\mathbf{Y}^{(0)}$;
for $t \leftarrow 0, 1, \cdots, T$ **do**
  update the gradient function $\Delta f\left(\mathbf{X}^{(t)}\right)$;
  update the step taken $\Delta\mathbf{X}^{(t)}$;
  update the gradient change $\Delta\mathbf{Y}^{(t)}$;
  update direction $\mathbf{D}^{(t+1)}$ with Algorithm 1;
  search for the step size $\beta^{(t+1)}$ with Armijo [7];
  update the phase matrix $\mathbf{X}^{(t+1)}$ with (16);
end
compute the designed waveform $\mathbf{s}_m^k = \exp\left(\mathrm{j}\mathbf{G}\mathbf{x}_{\mathrm{m}}^{\mathrm{k}}\right)$;

To address the challenges above, we employ an optimization strategy that approximates second-order information using a limited amount of first-order data. In this strategy, we adopt a technique based on limited-memory Broyden–Fletcher–Goldfarb–Shanno (L-BFGS) [52] to enhance the convergence rate and solution quality without significantly increasing computational complexity. Specifically, we approximate the Hessian matrix using historical information from past gradients and step sizes. Then, the descent direction at the $(t+1)$-th iteration can be given by

$$\mathbf{D}_{t+1} = -\mathbf{H}_{t+1}\nabla f(\mathbf{X}_t) \tag{17}$$

where $\mathbf{H}_{t+1}$ is the approximated inverse Hessian at the $(t+1)$th iteration, and $\nabla f(\mathbf{X}_t)$ is the gradient at the tth iteration. By storing no more than z pairs of the step taken and the change in the gradient, the approximation of the inverse Hessian can be updated using the following manner [53]:

$$\begin{aligned}\mathbf{H}_{t+1} = &\left(\mathbf{V}_t^T \cdots \mathbf{V}_{t-\hat{z}}^T\right)\mathbf{H}_t^0\left(\mathbf{V}_{t-z}\cdots\mathbf{V}_t\right)\\ &+ \rho_{t-\hat{z}}\left(\mathbf{V}_t^T\cdots\mathbf{V}_{t-\hat{z}+1}^T\right)\Delta\mathbf{X}_{t-\hat{z}}\Delta\mathbf{X}_{t-\hat{z}}^T\left(\mathbf{V}_{t-\hat{z}+1}\cdots\mathbf{V}_t\right)\\ &+\cdots+\rho_t\Delta\mathbf{X}_t\Delta\mathbf{X}_t^T\end{aligned} \tag{18}$$

where $\mathbf{H}_t^0$ is a predefined symmetric positive definite (SPD) matrix [54]. Here, we initialize $\mathbf{H}_t^0$ as the identity matrix at each iteration. $\mathbf{V}_t = \mathbf{I} - \rho_t\Delta\mathbf{Y}_t\Delta\mathbf{X}_t^T$, $\rho_k = 1/\langle\Delta\mathbf{X}_t, \Delta\mathbf{Y}_t\rangle$, $\hat{z} = \min\{t, z-1\}$, $\Delta\mathbf{X}_t = \mathbf{X}_{t+1} - \mathbf{X}_t$ is the step taken, and $\Delta\mathbf{Y}_t = \nabla f(\mathbf{X}_{t+1}) - \nabla f(\mathbf{X}_t)$ represents the change in the gradient. During implementation, (17) and (18) are jointly utilized to determine the descent direction at each step of the L-BFGS method. Algorithm 1 leverages these equations to implement a two-loop recursion strategy, which computes the search direction $\mathbf{D}_{t+1} = -\mathbf{H}_{t+1}\nabla f(\mathbf{X}_{t+1})$ without the need to explicitly store the matrix $\mathbf{H}_t$. This approach ensures computational efficiency while maintaining the accuracy of the optimization process.

With the Algorithm 1 at hand, the update rule in (16) allows the Hessian approximation to capture second-order behavior by using only first-order information from the previous iterations. By iteratively refining the approximation, the method accelerates convergence while controlling the computational cost. This approach effectively strikes a balance between the efficiency of first-order methods and the faster convergence typically associated with second-order optimization techniques. The steps of the proposed algorithm for the design of the complementary PCFM waveform are summarized in Algorithm 2. By iterating the update process in (16), the phase matrix is progressively refined until convergence is reached. K Termination criteria, such as limiting the number of iterations, monitoring gradient norms, or assessing the difference between consecutive objective function values can be used to stop the algorithm. In this work, the number of iterations is chosen. Specifically, when the number of iterations reaches a predetermined value T, the iteration process stops, and the optimized phase matrix $\mathbf{X}$ is output. As observed in Algorithms 1 and 2, at each iteration, it is necessary to compute the gradient at the current and previous iterations. Therefore, the gradient function is an indispensable element of the algorithm. Considering the stacking manner in (15), the gradient of the objective function can also be stacked in the same manner. Thus, we have

$$\nabla f(\mathbf{X}) = \begin{bmatrix} \frac{\partial}{\partial\mathbf{x}_1^1} f(\mathbf{X}) & \cdots & \frac{\partial}{\partial\mathbf{x}_M^1} f(\mathbf{X}) \\ \vdots & \ddots & \vdots \\ \frac{\partial}{\partial\mathbf{x}_1^K} f(\mathbf{X}) & \cdots & \frac{\partial}{\partial\mathbf{x}_M^K} f(\mathbf{X}) \end{bmatrix}_{KN\times M} \tag{19}$$

where $\frac{\partial}{\partial\mathbf{x}_m^k} f(\mathbf{X})$ is the partial derivative of the function $f(\mathbf{X})$ with respective to the phase vector $\mathbf{x}_m^k$, and its detailed expression and the computation process can be found in the Appendix.

B. Computational Complexity

The overall computational burden of the proposed method exhibits a linear relationship with the number of iterations. For each iteration, the computational complexity arises from the calculation of the gradient function, the evaluation of the cost function, and the approximation of the inverse Hessian matrix. Specifically, the overall computational complexity encompasses three primary components.

1) *Gradient Function:* The gradient matrix of the objective function is formed by stacking the partial derivatives of $K \times M$ terms, with each partial derivative being the sum of the partial derivatives corresponding to four subfunctions. In the calculation of each partial derivative, the dominant computation burden arises from the calculation of the autocorrelation function between different sequences, which can be efficiently computed using the FFT operation. Specifically, the computational complexity of the partial derivatives related to subfunctions $f_1(\mathbf{X})$ and $f_3(\mathbf{X})$ is $\mathcal{O}(KL\log L)$. In addition, the partial derivatives related to subfunctions $f_2(\mathbf{X})$ and $f_4(\mathbf{X})$ involve summing over the channel terms, resulting in a computational complexity of $\mathcal{O}(KML\log L)$. In summary, the overall computational complexity required to compute the gradient function is $\mathcal{O}(KML\log L)$.
2) *Cost Function:* The computational complexity of the cost function is influenced by the different subfunction components it comprises, each incorporating a sum of varying numbers of terms related to the Fourier transform. Given that the computational complexity of the Fourier transform is $\mathcal{O}(L\log L)$, the complexities of subfunctions $f_1(\mathbf{X})$ and $f_3(\mathbf{X})$ are $\mathcal{O}(KML\log L)$. Similarly, the complexities of subfunctions f_2 and f_4 are $\mathcal{O}(KM^2L\log L)$. Consequently, the overall computational complexity of the objective function is $\mathcal{O}(KM^2L\log L)$.
3) *Approximation of Inverse Hessian:* The computation of the approximate inverse Hessian matrix is embedded within the two-loop recursion process of Algorithm 1. The computational complexity of Algorithm 1 is primarily dominated by the inner product operations, each of which has a complexity of $\mathcal{O}(KMN)$. Given that the algorithm involves two nested loops, the overall computational complexity of the approximate inverse Hessian matrix calculation is approximately $\mathcal{O}(zKMN)$.

IV. NUMERICAL EXPERIMENTS

In this section, we assess the effectiveness of the proposed method for complementary PCFM waveform design in suppressing SMSP. The experimental setup is implemented using MATLAB R2022 on a personal computer equipped with a 2.30 GHz i7-112700H CPU and 40 GB of RAM.

A. Convergence of the Proposed Method

In this section, we begin by evaluating the convergence characteristics of the proposed method. The experiment is conducted using a complementary PCFM waveform set with parameters $M = 3$ and $N = 128$. The number of pulses within each CPI is set to 8, and the oversampling factor Q is set to 2. For the SMSP jamming parameters, the subpulse sample length is set to $\bar{L} = 64$, resulting in a downsampling rate of $P = 4$. The shift matrix $\mathbf{J}$ for SMSP jamming is subsequently determined using (1). In the waveform design process outlined in Algorithm 2, the maximum number of iterations is set to $T = 5000$. In addition, the phase matrix is initialized using random variables drawn from a uniform distribution over the interval $[0, 2\pi]$.

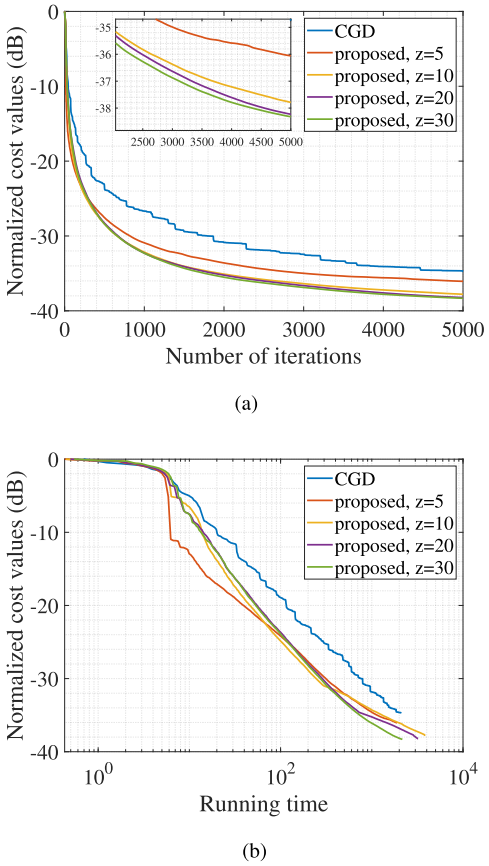

Fig. 2. Convergence performance comparison of the proposed method with different memory sizes. (a) Cost values with the number of iterations. (b) Cost values with the running time (sec).

We first explore the influence of the memory size (the number of stored step pairs z) on the convergence performance of the proposed method. Fig. 2 presents the cost values as a function of the number of iterations and running time for memory sizes $z = 5$, 10, 20, 30. To demonstrate the superiority of the proposed algorithm, the convergence behaviors of the CGD algorithm is also included for comparison. As illustrated in Fig. 2(a), all algorithms exhibit a monotonically decreasing trend across all configurations. Compared to the convergence curve of the CGD algorithm, the curve for the proposed method is smoother, converges more rapidly, and reaches a lower final value. Examining the convergence curves for different memory sizes z, it is evident that as z increases, the optimization performance of the algorithm improves, primarily reflected in the lower convergence values. In addition, as shown in Fig. 2(b), the required running time increases with the growth of z. This indicates that, in practical applications, the memory size should be carefully selected based on the specific problem model to strike an optimal balance between optimization performance and computational efficiency. In the following experiments of this section, we fix the memory size at $z = 20$

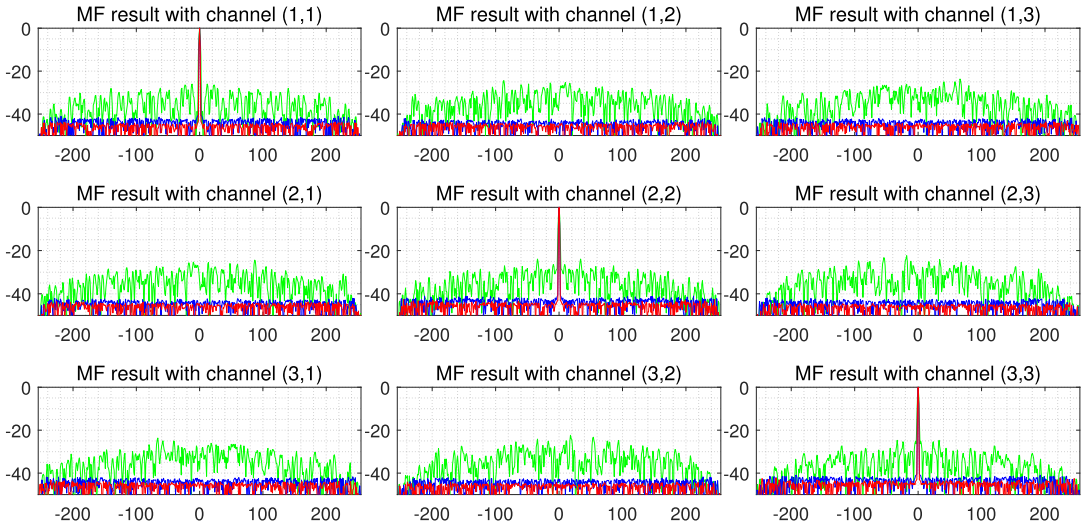

(a)

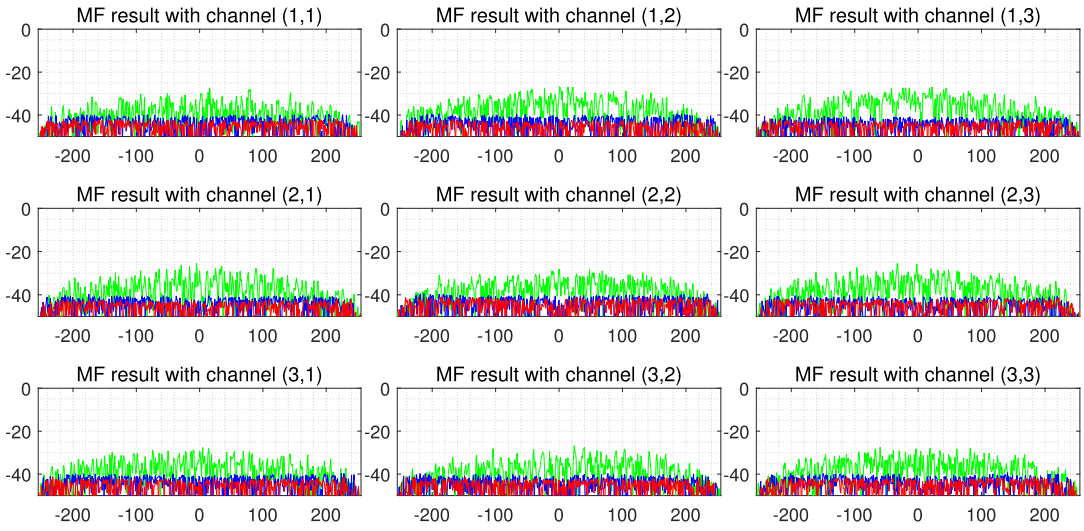

(b)

Fig. 3. Complementary MF results for waveforms from different channels and waveform-SMSP pairs from different channels. For each subfigure, the horizontal axis represents the range bins, and the vertical axis represents the normalized response value in dB. In addition, the red and blue results correspond to the proposed method and the CGD method, respectively. The green results correspond to the initial waveform. (a) Complementary MF results with waveform-waveform pairs from different channels. (b) Complementary MF results with waveform-SMSP pairs from different channels.

to balance the convergence performance and computational complexity.

To visually assess the performance of the designed complementary PCFM waveform set, we present the complementary MF results for various waveform-waveform pairs and waveform-SMSP pairs across distinct channels. As shown in Fig. 3(a), the complementary MF results for the PCFM waveforms within the same channel exhibit pronounced peaks at the zero-delay position, accompanied by a peak-to-sidelobe level (PSL) of approximately 40 dB, demonstrating the robustness of the PC performance. In contrast, the complementary MF results for PCFM waveforms from different channels do not exhibit significant peaks, emphasizing the effectiveness of the optimized PCFM waveforms in mitigating inter-channel interference. To further illustrate the effectiveness of the designed complementary PCFM waveforms in SMSP suppression, we also present the complementary MF results for waveform-SMSP pairs from different channels in Fig. 3(b). Notably, these results show relatively small peaks (around 40 dB) for both same- and different-channel configurations, underscoring the method's efficacy in reducing the influence caused by the SMSP jamming. Furthermore, in most cases, the sidelobe levels and SMSP response values achieved by the proposed method are lower than those obtained with the CGD method, highlighting the superior performance of our proposed complementary waveform design approach in SMSP suppression. In addition, since different algorithms

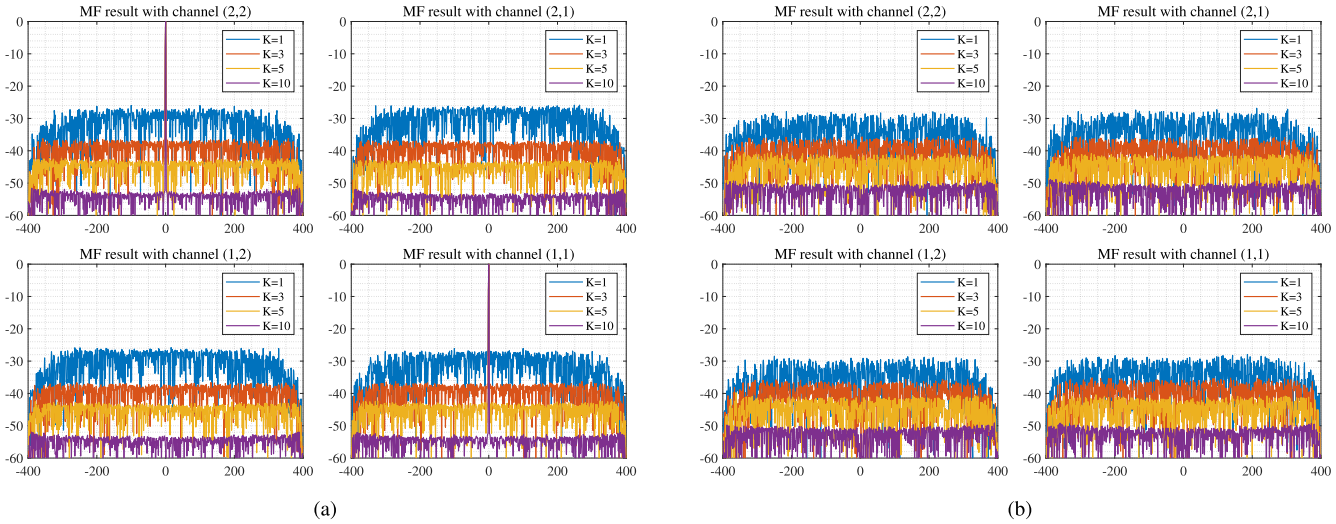

Fig. 4. Complementary MF results under different settings of K. For each subfigure, the horizontal and vertical axes represent the range bins and the normalized response value in dB. (a) Complementary MF results with waveform-waveform pairs from different channels. (b) Complementary MF results with waveform-SMSP pairs from different channels.

use different strategies to obtain suboptimal solutions, and the final objective function values of these suboptimal solutions tend to be relatively close to each other, the performance improvement observed in Fig. 3 is limited. However, in comparison to the initial waveforms, the designed PCFM waveforms exhibit significantly improved PC performance and superior SMSP suppression performance, thereby validating the effectiveness of the proposed waveform design method. Furthermore, the convergence curves of the objective function, as depicted in Fig. 2, provide additional evidence of the method's superiority, demonstrating its optimization capability and efficiency in achieving the desired performance metrics.

B. Influence of Waveform and SMSP Parameters

To comprehensively evaluate the influence of waveform variations and SMSP jamming parameters, we perform a systematic analysis of how the pulse number K within each CPI, the phase code length N within each pulse, and the downsampling factor P collectively impact the overall waveform performance. Notably, since the dimension of the optimization variable is governed by M, N, and K, the parameter Q does not directly affect the optimization process. Consequently, the discussion regarding the influence of Q is excluded from this analysis. This focused approach allows us to isolate and examine the key parameters that drive waveform performance under SMSP jamming conditions.

We begin by examining the PCFM waveform design process for different pulse number settings: $K = 1, 3, 5, 10$. In these experiments, the coding length N is fixed at 200, the channel number M is set to 2, and other parameters related to the waveform and PCFM jamming are consistent with those used in the previous sections. Fig. 4 illustrates the complementary MF results for varying values of K. As shown in Fig. 4(a), the PCFM waveforms from the same channel exhibit high peak values, while those from different channels show minimal cross-correlation levels. Furthermore, as shown in Fig. 4(b), for the complementary MF results across all waveform-SMSP pairs, whether from the same or different channels, no significant peaks are observed, confirming the effectiveness of the proposed method in SMSP suppression. More notably, as the pulse number K increases, the sidelobes of the waveform, cross-correlation levels, and SMSP response levels all decrease progressively. Specifically, when K increases from 1 to 10, these metrics show an approximate reduction of 20 dB, indicating improved performance in both target detection and SMSP suppression. This suggests that a higher value of K further enhances waveform performance. The optimal choice of K can therefore be determined based on the specific jamming environment, where a larger K generally yields better results.

TABLE I
Performance Evaluation Metrics in dB With $M = 2$ and $N = 64$

	$P = 4$	$P = 8$	$P = 16$	$P = 32$
PSL	-32.02	-33.21	-34.68	-35.11
CCP	-32.23	-33.64	-34.66	-36.08
PSMSP	-30.55	-34.15	-36.52	-38.47

We further explore the impacts of waveform coding length N and SMSP downsampling factor P on the waveform performance. We select two channels $M = 2$ and adjust the coding length N to 64, 128, 256, and 512. For each CPI, the waveform number K is set to 3. For the SMSP parameters, the downsampling factor P is varied in the range of 4, 8, 16, and 32. All other parameters relevant to the proposed method are maintained consistent with those detailed in the preceding section. Tables I–IV provide a comprehensive evaluation of the waveform design metrics, including PSL, CCP, and peak of SMSP (PSMSP),

TABLE II
Performance Evaluation Metrics in dB With $M = 2$ and $N = 128$

	$P = 4$	$P = 8$	$P = 16$	$P = 32$
PSL	-33.97	-35.49	-35.83	-37.64
CCP	-35.25	-36.28	-36.49	-38.38
PSMSP	-33.51	-36.14	-38.27	-41.36

TABLE III
Performance Evaluation Metrics in dB With $M = 2$ and $N = 256$

	$P = 4$	$P = 8$	$P = 16$	$P = 32$
PSL	-37.25	-37.96	-39.05	-40.16
CCP	-37.35	-38.44	-39.06	-40.68
PSMSP	-36.37	-38.30	-40.80	-44.58

TABLE IV
Performance Evaluation Metrics in dB With $M = 2$ and $N = 512$

	$P = 4$	$P = 8$	$P = 16$	$P = 32$
PSL	-38.22	-39.10	-40.69	-40.26
CCP	-39.39	-40.33	-41.45	-40.81
PSMSP	-38.35	-41.06	-43.37	-44.05

under varying parameters of the downsampling rate P and phase coding length N. We need to point out that CCP represents the peak value of the cross-correlation between waveforms of different channels, while PSMSP refers to the peak response generated by an arbitrary waveform-SMSP pair. As P increases, all three metrics exhibit a consistent improvement, with PSL and CCP demonstrating a gradual reduction, indicating enhanced suppression of sidelobe and cross-correlation peaks. The PSMSP metric shows a more pronounced improvement with larger P, particularly at $P = 16$ and $P = 32$, highlighting its sensitivity to the downsampling rate and its critical role in mitigating SMSP jamming. Furthermore, increasing N leads to significant improvements across all metrics, emphasizing the benefits of longer phase coding in enhancing waveform performance. Notably, the improvements in PSMSP are especially substantial for larger N, such as $N = 256$ and $N = 512$, underscoring the importance of longer phase coding lengths in addressing SMSP jamming. These results demonstrate that both larger P and N contribute to improved waveform design, with N exerting a more consistent impact across all metrics, while P plays a crucial role in enhancing PSMSP performance. Explaining from the mathematical principles of the established PCFM waveform design model, this outcome stems from the enhanced design flexibility afforded by longer waveforms and the diminished coherence of jamming signals with more subpulses. This analysis provides valuable insights for optimizing waveform parameters to achieve superior performance.

TABLE V
Parameter Settings of the SMSP Jammer and Target

SMSP and target parameters	Values
SMSP subpulse width	$5\,\mu$s
SMSP location	1.3, 1.4, 1.5 km
Target location	1.0, 1.2 km
Signal to Jamming ratio (SJR)	-30 dB

C. SMSP Suppression for Target Detection

To further demonstrate the superiority of the proposed complementary PCFM waveform design method in SMSP jamming suppression, we conducted a target detection experiment in the SMSP jamming environment. For the waveform parameters, we set the PCFM pulse duration to 20 μs, and the waveform sampling rate as 10 MHz. For the SMSP jamming parameters, the downsampling factor is set as $P = 4$, the jammer forwarding delay is set as 1 μs, and the distance between the radar system and the SMSP jammer is 1 km. The specific parameter settings for the targets and the SMSP jammer are outlined in Table V. It is assumed that the SMSP jammer retransmits the captured radar waveforms with three distinct time delays after the jamming signal is generated. This leads to the formation of three false targets at distances of 1.3 , 1.4 , and 1.5 km, respectively.

In Fig. 5, the PC results corresponding to various SMSP jamming conditions and waveform configurations are presented to evaluate the performance of SMSP suppression and target detection. Since existing methods do not address SMSP suppression in multichannel radar systems, we employ a two-channel radar system for comparison with the designed complementary PCFM waveforms. In this system, each channel transmits LFM waveforms with opposite chirp rates, namely, 1.0 and -1.0 MHz / us, respectively. Fig. 5(a) and (b) show the PC results for the LFM waveforms in an SMSP-free environment. As observed, two prominent targets are easily identifiable due to their high peaks compared to the sidelobe levels. However, when SMSP jamming is introduced into the transmit LFM waveforms, the sidelobe levels increase significantly, potentially leading to target detection failure, as depicted in Fig. 5(c) and (d). Fig. 5(e) and (f) present the PC results for the phase-coded waveforms in the presence of SMSP. As illustrated, both preset targets are clearly detectable, with the highest sidelobe level measured at -13.79 dB. However, under the SMSP jamming scenario, as depicted in Fig. 5(g) and (h), the sidelobe levels rise substantially, effectively masking the true targets. This contrast highlights the significant impact of SMSP jamming on target detection performance, underscoring the challenges posed by such jamming in radar systems. In contrast, Fig. 5(i) and (j) present the PC results for the complementary PCFM waveforms with $K = 1$. In these cases, the sidelobe levels induced by the SMSP jamming are effectively suppressed, enhancing the radar system's performance in the presence of SMSP jamming. Furthermore, as illustrated in Fig. 5(k) and (l), the sidelobe levels are further reduced,

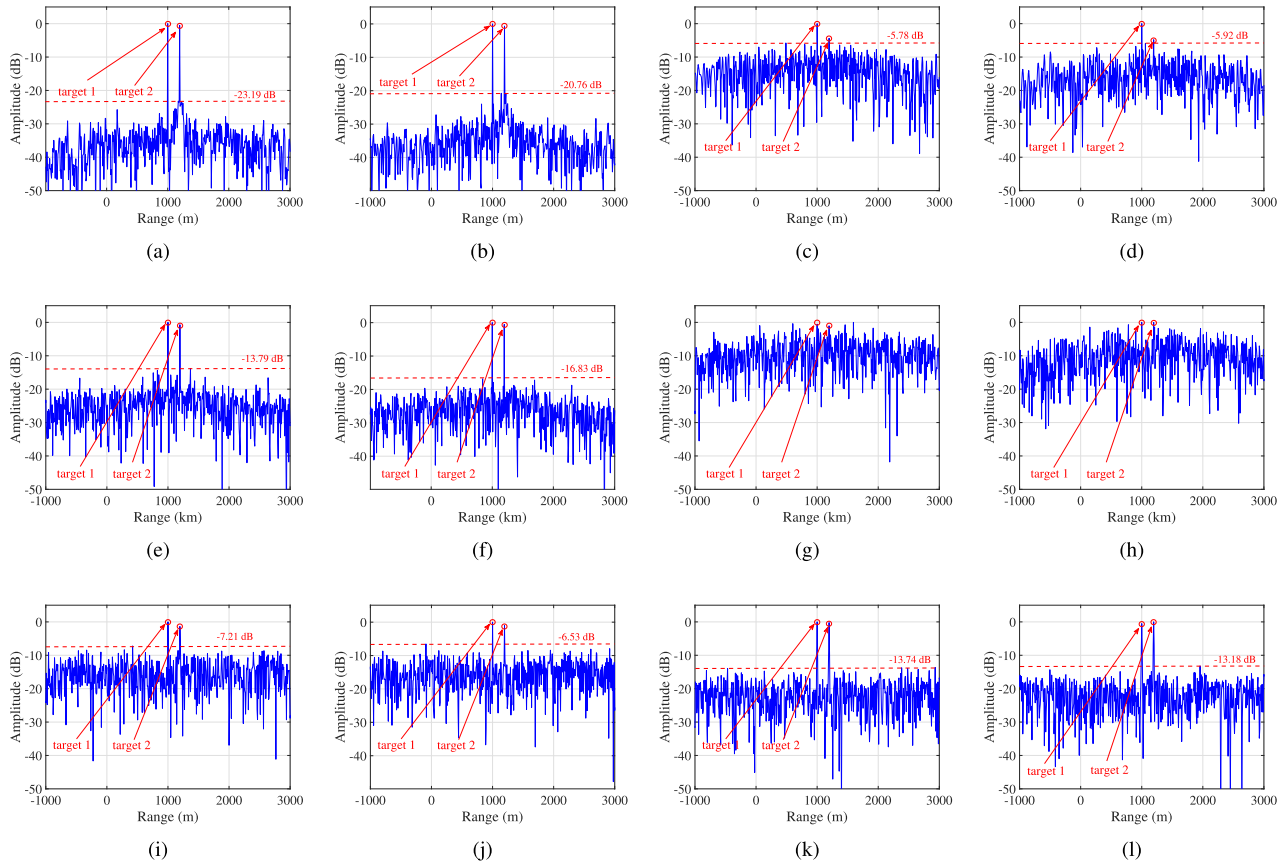

Fig. 5. Experimental results of SMSP suppression and target detection under the SMSP jamming scenario. (a)–(b) PC results for LFM waveforms in the SMSP-free scenario, corresponding to channels 1 and 2, respectively. (c)–(d) PC results for LFM waveforms under the SMSP scenario, associated with channels 1 and 2. (e)–(f) PC results for phase-coded waveforms in the SMSP-free scenario, evaluated for channels 1 and 2. (g)–(h) PC results for phase-coded waveforms under the SMSP scenario, corresponding to channels 1 and 2. (i)–(j) PC results for the complementary PCFM waveforms with $K = 1$ under the SMSP scenario, analyzed for channels 1 and 2. (k)–(l) PC results for the complementary PCFM waveforms with $K = 3$ under the SMSP scenario, evaluated for channels 1 and 2.

reaching approximately -13 dB, indicating improved anti-SMSP performance with a larger K. It is anticipated that as K increases, the SMSP suppression capability of the radar system improves, offering significant potential for further advancements in SMSP jamming mitigation.

D. SMSP Suppression for Radar Imaging

The high-resolution range profile (HRRP) of captures the combined contributions of target scattering points projected along the radar's line-of-sight direction. It serves as a valuable source of information for characterizing target structure and scattering patterns. Compared to 2-D synthetic aperture radar (SAR) and inverse SAR (ISAR) images, 1-D HRRP data are not only easier to acquire but also applicable to a broader range of scenarios, making it a practical choice for target recognition and analysis [55]. In this subsection, we assess the performance of the PCFM waveform design method in suppressing SMSP for radar imaging applications. To conduct the experiment, we first construct a computer-aided design (CAD) model of an aircraft. Using electromagnetic simulation software, we compute the radar cross section (RCS) data of the target. Fig. 6(a) illustrates the CAD model, while Fig. 6(b) displays the computed RCS data at an elevation of 45° and an azimuth of 75°. Based on the obtained RCS data, we simulate the radar echo corresponding to various transmit waveforms, enabling the generation of the aircraft's HRRP. For the experiments, the transmit waveform parameters are configured as follows: The carrier frequency is set to 10 GHz, the pulse width is 2.5 μs, and the sampling rate is 100 MHz. The SMSP settings remain consistent with those used in the previous subsection. This setup allows us to systematically evaluate the effectiveness of the PCFM waveform in mitigating ISRJ and enhancing radar imaging performance.

In Fig. 6(c)–(h), we present the realized HRRPs realized by the LFM waveform, the phase-coded waveform, and the designed PCFM waveform. Specifically, the results shown in Fig. 6(d) and (f) employ the SMSP countermeasures introduced in [21]. Based on the experimental results, it is evident that the presence of SMSP significantly degrades radar imaging performance, primarily manifested in the elevation of sidelobes and the masking of weak scattering points. Although the signal reconstruction-based method illustrated in Fig. 6(d) and (f) can partially cancel the SMSP

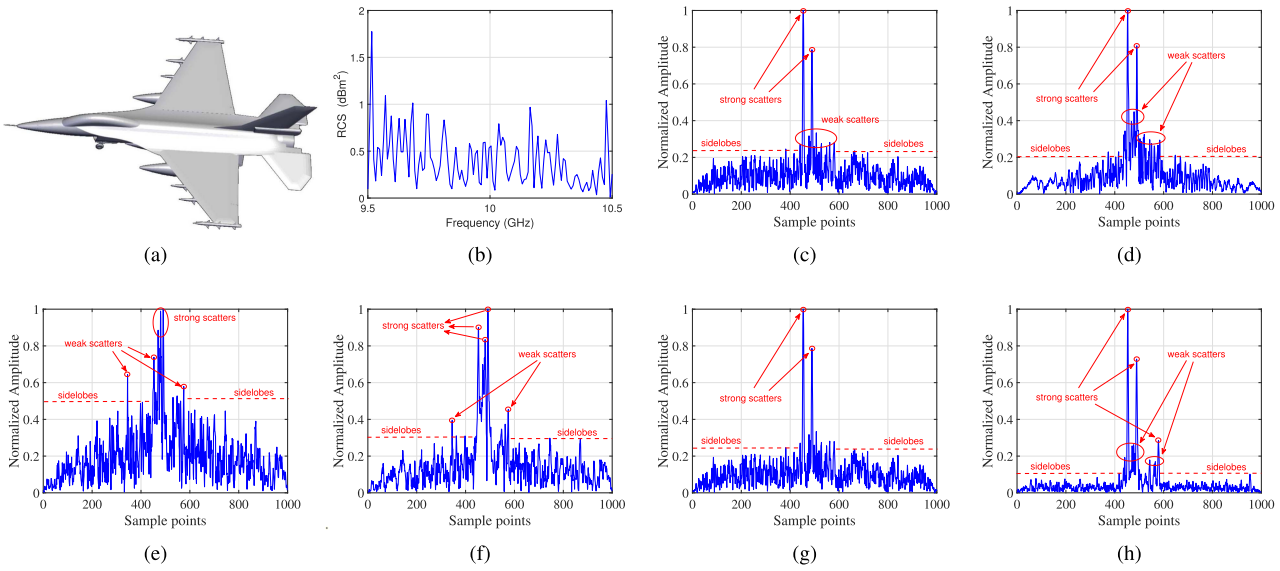

Fig. 6. (a)–(b) CAD model of the aircraft and corresponding RCS amplitude data. (c)–(d) Realized HRRPs of the LFM waveform. (e)–(f) Realized HRRPs of the phase-coded waveform. (g)–(h) Realized HRRPs of the PCFM waveform for $K = 1$ and $K = 3$.

components, the residual sidelobe levels still severely impact the detection of weak scattering points. In contrast, the proposed PCFM waveform demonstrates superior performance by enhancing SMSP suppression through an increase in the number of complementary pulses. When $K = 3$, the sidelobe regions in the HRRP are significantly suppressed, and weak scattering points become distinctly visible. This clearly highlights the advantages of the proposed method in radar imaging applications.

E. Influence of the Missed Pulses

In practice, both the radar receiver and the SMSP jammer may miss certain pulses due to hardware limitations and operational constraints. To investigate the impact of these missed pulses, we conducted a target detection experiment under SMSP jamming conditions. The waveform parameters are configured as follows: $M = 1$, $N = 100$, $K = 5$, and $Q = 4$. In addition, the pulse width is set to $20\,\mu s$, and the sampling rate is fixed at 20 MHz. For the jamming parameters, the downsampling factor is set to $P = 4$, and the forwarding delay is $1\,\mu s$. The target is positioned 5 km from the radar system, while the SMSP jammer is placed 5.5 -km away.

To analyze the effect of missed pulses on both the receiver and the jammer, we examine the realized signal-to-jamming ratio (SJR) as a function of the number of missed pulses. The results illustrated in Fig. 7 indicate that the highest SJR values are achieved when the SMSP jammer intercepts all pulses and the radar receives all echoes. However, as the number of missed pulses due to incomplete reception increases, the realized SJR declines significantly. This phenomenon can be due to the disruption of the coherent design among complementary pulses, which diminishes the effectiveness of SMSP suppression during

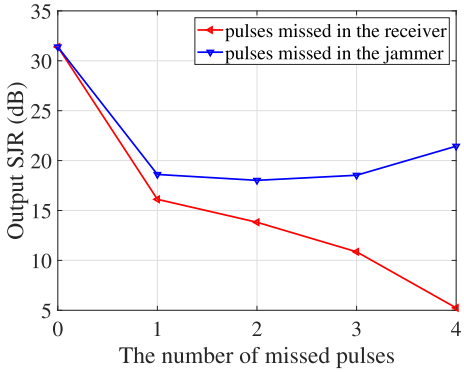

Fig. 7. Realized SJRs with different missed pulses.

pulse processing. Interestingly, when the number of missed pulses caused by the SMSP jammer increases, the realized SJR initially decreases but subsequently rises. The initial decline is due to the destruction of phase coherence between pulses, while the subsequent increase is a result of reduced jamming energy entering the receiver as fewer jamming pulses are transmitted.

In summary, when employing complementary PCFM for SMSP suppression, it is crucial to ensure that both the radar and the jammer receive all pulses within a CPI. If complete reception cannot be guaranteed, a practical solution is to reduce the number of pulses in the complementary PCFM waveform set, thereby lowering the stringent reception requirements of the proposed method. To validate the effectiveness of the proposed method under extreme conditions, we reconfigure the number of pulses to $K = 1$ and redesign the waveforms accordingly. The PC results for the newly designed waveform, along with those for LFM waveforms, are presented in Fig. 8. As demonstrated, the

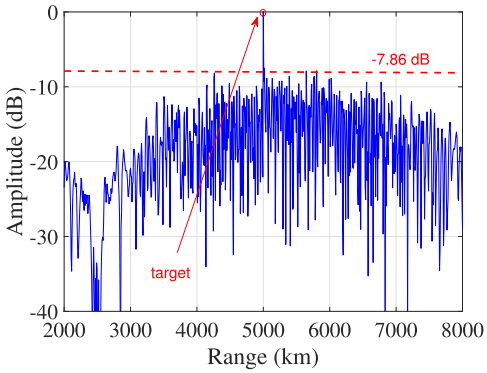

(a)

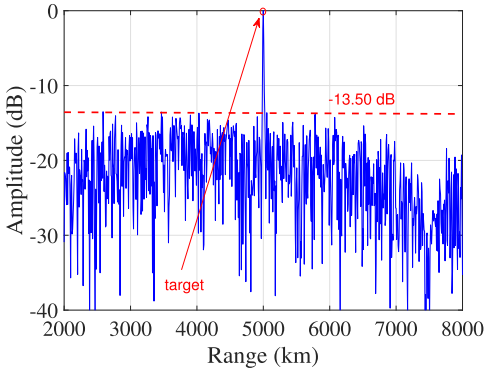

(b)

Fig. 8. Experimental results of target detection under the SMSP jamming environment. (a) PC result of the LFM waveform. (b) PC result of the PCFM waveform.

proposed method achieves superior jamming suppression performance in SMSP jamming scenarios, confirming its effectiveness.

F. Analysis of the Parameter Sensitivity

As shown in Section II, the established complementary PCFM waveform design model relies on the prior information of SMSP jamming. Since the SMSP parameters are determined by the downsampling factor P, we evaluate the jamming suppression performance under the imperfect downsampling rate of the jammer. In this experiment, we consider a radar system equipped with two different channels, each transmitting the PCFM waveform with time width of 20 μs, and the sampling rate of 20 MHz. In addition, the complementary waveform number is set to $K = 3$, the coded length is set to $N = 100$, and the target is located 5 -km away from the radar system. For the target equipped SMSP jamming, forwarding delay is set to 1 μs, and the practical sampling rate is set to 5 MHz, resulting in a downsampling factor of $P = 4$.

In Fig. 9, the SJR across different channels is presented to evaluate the effectiveness of the proposed method under varying SMSP jamming parameters. The results show that when the jamming parameters are accurately estimated, the realized SJR achieves optimal jamming suppression

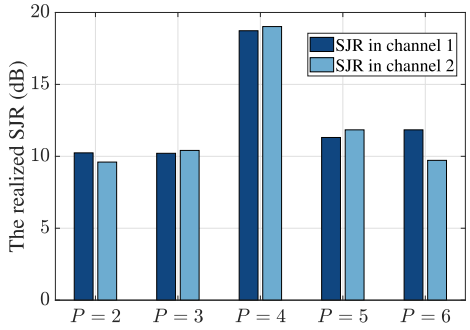

Fig. 9. Realized SJRs in different channels for varying downsample factors.

performance, reaching approximately 19 dB across all channels. However, as the estimation accuracy gets worse, the realized SJR degrades significantly, highlighting the critical importance of accurate prior information. Notably, even in scenarios where precise SMSP jamming parameters are unavailable, the proposed method still maintains an SJR of about 10 dB, confirming its robustness and practical applicability under imperfect conditions. These findings collectively demonstrate the method effectiveness in mitigating SMSP components, even with limited prior knowledge.

V. CONCLUSION

This study investigates the design of PCFM waveforms in MIMO radar systems for the suppression of SMSP jamming. To further enhance SMSP jamming suppression, multiple waveform pulses within each CPI are considered under a waveform complementary strategy. The problem of waveform design is initially formulated as a multiobjective optimization task, where the goal is to minimize a series of subfunctions. An iterative algorithm based on the approximation of the inverse Hessian is further employed to facilitate the optimization process, enabling an iterative search for the required PCFM waveform. Numerical experiments are then conducted to evaluate the effectiveness of the proposed approach.

The results of the proposed PCFM waveform design method demonstrate promising performance in SMSP jamming suppression. However, a major challenge in practical implementation arises from the assumption of prior knowledge regarding the parameters of SMSP jamming. Therefore, future research should focus on developing methods for estimating these parameters and enhancing the robustness of the anti-SMSP techniques through complementary PCFM waveform optimization. To reach this goal, the scope of waveform design could be further expanded by simultaneously optimizing both the transmit waveform and the receive filter. In addition, while the optimization method employed here relies on a traditional gradient-based algorithm that generates a descent direction using a linear mapping of the gradient function, future research could explore the use of nonlinear operators. Integrating learning-based algorithms into the optimization process could potentially

lead to more effective complementary PCFM waveforms with improved SMSP suppression capabilities.

APPENDIX

In this section, we present the calculation progress of the partial derivatives $\frac{\partial}{\partial \mathbf{x}_m^k} f(\mathbf{X})$. Then, the gradient function concerning the phase matrix $\mathbf{X}$ can be formed with the introduced stacking manner. Since $f(\mathbf{X})$ involves four different components, the partial derivative can be calculated as

$$\frac{\partial}{\partial \mathbf{x}_m^k} f(\mathbf{X}) = \frac{\partial}{\partial \mathbf{x}_m^k} f_1(\mathbf{X}) + \frac{\partial}{\partial \mathbf{x}_m^k} f_2(\mathbf{X}) + \frac{\partial}{\partial \mathbf{x}_m^k} f_3(\mathbf{X}) + \frac{\partial}{\partial \mathbf{x}_m^k} f_4(\mathbf{X}). \tag{20}$$

In the following parts, the expression of each partial derivative will be demonstrated.

A. Calculation of the Partial Derivative $\frac{\partial}{\partial \mathbf{x}_m^k} f_1(\mathbf{X})$

The partial derivative in this part can be computed using various methods. In this work, we utilize a strategy in which we first differentiate concerning a single PCFM parameter $\mathbf{x}_m^k(n)$, and then organize the expression to enable the parallel computation of the derivatives to all N PCFM parameters.

Making use of the fact that the elements of $\mathbf{w}_{\mathrm{SL}}$ and $\mathbf{w}_{\mathrm{ML}}$ contain only ones and zeroes, we have

$$\frac{\left\|\mathbf{w}_{\mathrm{SL}}^T \mathbf{r}_{mm}\right\|_p^2}{\left\|\mathbf{w}_{\mathrm{ML}}^T \mathbf{r}_{mm}\right\|_p^2} = \left(\frac{\mathbf{w}_{\mathrm{SL}}^T |\mathbf{r}_{mm}|^p}{\mathbf{w}_{\mathrm{ML}}^T |\mathbf{r}_{mm}|^p}\right)^{\frac{2}{p}}. \tag{21}$$

Then, by the chain rule, the partial derivative of $f_1(\mathbf{X})$ with respect to $\mathbf{x}_m^k(n)$ can be expressed as

$$\frac{\partial}{\partial \mathbf{x}_m^k(n)} f_1(\mathbf{X}) = \frac{\partial}{\partial \mathbf{x}_m^k(n)} \left(\frac{\mathbf{w}_{\mathrm{SL}}^T |\mathbf{r}_{mm}|^p}{\mathbf{w}_{\mathrm{ML}}^T |\mathbf{r}_{mm}|^p}\right)^{\frac{2}{p}} = \frac{2}{p}\left(\frac{\mathbf{w}_{\mathrm{SL}}^T |\mathbf{r}_{mm}|^p}{\mathbf{w}_{\mathrm{ML}}^T |\mathbf{r}_{mm}|^p}\right)^{\frac{2}{p}-1} \frac{\partial}{\partial \mathbf{x}_m^k(n)} \left(\frac{\mathbf{w}_{\mathrm{SL}}^T |\mathbf{r}_{mm}|^p}{\mathbf{w}_{\mathrm{ML}}^T |\mathbf{r}_{mm}|^p}\right). \tag{22}$$

Subsequently, we apply the chain rule to (22), then we have

$$\frac{\partial}{\partial \mathbf{x}_m^k(n)} \frac{\mathbf{w}_{\mathrm{SL}}^T |\mathbf{r}_{mm}|^p}{\mathbf{w}_{\mathrm{ML}}^T |\mathbf{r}_{mm}|^p} = \frac{\mathbf{w}_{\mathrm{SL}}^T |\mathbf{r}_{mm}|^p}{\mathbf{w}_{\mathrm{ML}}^T |\mathbf{r}_{mm}|^p} \times \left(\frac{\mathbf{w}_{\mathrm{SL}}^T}{\mathbf{w}_{\mathrm{SL}}^T |\mathbf{r}_{mm}|^p} \frac{\partial |\mathbf{r}_{mm}|^p}{\partial \mathbf{x}_m^k(n)} - \frac{\mathbf{w}_{\mathrm{ML}}^T}{\mathbf{w}_{\mathrm{ML}}^T |\mathbf{r}_{mm}|^p} \frac{\partial |\mathbf{r}_{mm}|^p}{\partial \mathbf{x}_m^k(n)}\right). \tag{23}$$

To obtain the partial derivative of $\mathbf{r}_{mm}$, we employ both the chain rule and the product rule, which yields

$$\begin{aligned}
&\frac{\partial}{\partial \mathbf{x}_m^k(n)} |\mathbf{r}_{mm}|^p \\
&= \frac{\partial}{\partial \mathbf{x}_m^k(n)} \left(\mathbf{r}_{mm} \odot \mathbf{r}_{mm}^*\right)^{\frac{p}{2}} \\
&= \frac{p}{2} |\mathbf{r}_{mm}|^{\frac{p-2}{2}} \odot \left(\frac{\partial \mathbf{r}_{mm}}{\partial \mathbf{x}_m^k(n)} \odot \mathbf{r}_{mm}^* + \mathbf{r}_{mm} \odot \frac{\partial \mathbf{r}_{mm}^*}{\partial \mathbf{x}_m^k(n)}\right) \\
&= p |\mathbf{r}_{mm}|^{p-2} \odot \mathrm{Re}\left(\frac{\partial \mathbf{r}_{mm}}{\partial \mathbf{x}_m^k(n)} \odot \mathbf{r}_{mm}^*\right).
\end{aligned} \tag{24}$$

Since the FFT matrix denotes a linear operator here, the partial derivative of $\mathbf{r}_{mm}$ becomes

$$\begin{aligned}
\frac{\partial \mathbf{r}_{mm}}{\partial \mathbf{x}_m^k(n)} &= \frac{\partial}{\partial \mathbf{x}_m^k(n)} \left[\mathbf{F}^H \left(\left(\mathbf{F}\bar{\mathbf{s}}_m^k\right) \odot \left(\mathbf{F}\bar{\mathbf{s}}_m^k\right)^*\right)\right] \\
&= 2\mathbf{F}^H \mathrm{Re}\left[\left(\mathbf{F}\bar{\mathbf{s}}_m^k\right) \odot \left(\mathbf{F} \frac{\partial \bar{\mathbf{s}}_m^k}{\partial \mathbf{x}_m^k(n)}\right)^*\right]
\end{aligned} \tag{25}$$

after once again employing the product rule. Using the compact expression in (6), the nonzero portion of the derivative in (25) turn to be

$$\frac{\partial \mathbf{s}_m^k}{\partial \mathbf{x}_m^k(n)} = \frac{\partial}{\partial \mathbf{x}_m^k(n)} \exp\left(j\mathbf{G}\mathbf{x}_m^k\right) = j\mathbf{g}_n \odot \mathbf{s}_m^k \tag{26}$$

where $\mathbf{g}_n$ is the nth column of $\mathbf{G}$. Further, the zero-padded form of derivative in (25) can be obtained via

$$\frac{\partial \bar{\mathbf{s}}_m^k}{\partial \mathbf{x}_m^k(n)} = j\bar{\mathbf{g}}_n \odot \bar{\mathbf{s}}_m^k \tag{27}$$

in which $\bar{\mathbf{g}}_n$ is the zero-padded version of $\mathbf{g}_n$ with dimension of $(2L-1) \times 1$. By substituting (27) into (25) and then substituting the resulting expression into (24), we can obtain

$$\mathbf{w}_{\mathrm{SL}}^T \frac{\partial}{\partial \mathbf{x}_m^k(n)} |\mathbf{r}_{mm}|^p = 2p\bar{\mathbf{g}}_n^T \mathrm{Im}\left\{\left(\bar{\mathbf{s}}_m^k\right)^* \odot \left(\mathbf{F}^H \left[\mathbf{F}\left(\mathbf{w}_{\mathrm{SL}} \odot |\mathbf{r}_{mm}|^{p-2} \odot \mathbf{r}_{mm}\right) \odot \left(\mathbf{F}\bar{\mathbf{s}}_m^k\right)\right]\right)\right\} \tag{28}$$

after some mathematical manipulations. By substituting (28) into (22), we can obtain the partial derivative of the function $f_1(\mathbf{X})$ with respect to $\mathbf{x}_m^k(n)$. Furthermore, by stacking the partial derivatives of the N elements columnwise and defining $\bar{\mathbf{G}} = [\bar{\mathbf{g}}_1, \ldots, \bar{\mathbf{g}}_N]$, we can derive the partial derivative of $f(\mathbf{X})$ with respect to the phase vector $\mathbf{x}_m^k$, as follows: (29) shown at the bottom of this page.

B. Calculation of the Partial Derivative $\frac{\partial}{\partial \mathbf{x}_m^k} f_2(\mathbf{X})$

Since the subobjective function $f_2(\mathbf{X})$ involves two summation operations, its gradient can be decoupled into the

$$\frac{\partial}{\partial \mathbf{x}_m^k} f_1(\mathbf{X}) = 4\left(\frac{\mathbf{w}_{\mathrm{SL}}^T |\mathbf{r}_{mm}|^p}{\mathbf{w}_{\mathrm{ML}}^T |\mathbf{r}_{mm}|^p}\right)^{\frac{2}{p}} \bar{\mathbf{G}}^T \times \mathrm{Im}\left\{\left(\bar{\mathbf{s}}_m^k\right)^* \odot \left(\mathbf{F}^H \left[\mathbf{F}\left(\left[\frac{\mathbf{w}_{\mathrm{SL}}}{\mathbf{w}_{\mathrm{SL}}^T |\mathbf{r}_{mm}|^p} - \frac{\mathbf{w}_{\mathrm{ML}}}{\mathbf{w}_{\mathrm{ML}}^T |\mathbf{r}_{mm}|^p}\right] \odot |\mathbf{r}_{mm}|^{p-2} \odot \mathbf{r}_{mm}\right) \odot \left(\mathbf{F}\bar{\mathbf{s}}_m^k\right)\right]\right)\right\}. \tag{29}$$

following two summation terms:

$$\frac{\partial}{\partial \mathbf{x}_m^k(n)} f_2(\mathbf{X}) = \sum_{m'=1}^{M} \frac{\partial}{\partial \mathbf{x}_m^k(n)} \frac{\|\mathbf{r}_{m'm}\|_p^2}{\|\mathbf{r}_{m'm'} \odot \mathbf{w}_{\mathrm{ML}}\|_p^2} + \sum_{m'=1}^{M} \frac{\partial}{\partial \mathbf{x}_m^k(n)} \frac{\|\mathbf{r}_{m'm}\|_p^2}{\|\mathbf{r}_{m'm'} \odot \mathbf{w}_{\mathrm{ML}}\|_p^2}. \quad (30)$$

For the term within the first summation operation, we have

$$\begin{aligned}
&\frac{\partial}{\partial \mathbf{x}_m^k(n)} \frac{\|\mathbf{r}_{mm'}\|_p^2}{\|\mathbf{r}_{mm} \odot \mathbf{w}_{\mathrm{ML}}\|_p^2} \\
&= \frac{2}{p}\left(\frac{\mathbf{1}^T|\mathbf{r}_{mm'}|^p}{\mathbf{w}_{\mathrm{ML}}^T|\mathbf{r}_{mm}|^p}\right)^{\frac{2}{p}-1} \frac{\partial}{\partial \mathbf{x}_m^k(n)}\left(\frac{\mathbf{1}^T|\mathbf{r}_{mm'}|^p}{\mathbf{w}_{\mathrm{ML}}^T|\mathbf{r}_{mm}|^p}\right) \\
&= \frac{2}{p}\left(\frac{\mathbf{1}^T|\mathbf{r}_{mm'}|^p}{\mathbf{w}_{\mathrm{ML}}^T|\mathbf{r}_{mm}|^p}\right)^{\frac{2}{p}-1} \frac{\mathbf{1}^T|\mathbf{r}_{mm'}|^p}{\mathbf{w}_{\mathrm{ML}}^T|\mathbf{r}_{mm}|^p} \\
&\quad \times \left[\frac{\mathbf{1}^T}{\mathbf{1}^T|\mathbf{r}_{mm'}|^p}\frac{\partial|\mathbf{r}_{mm'}|^p}{\partial \mathbf{x}_m^k(n)} - \frac{\mathbf{w}_{\mathrm{ML}}^T}{\mathbf{w}_{\mathrm{ML}}^T|\mathbf{r}_{mm}|^p}\frac{\partial|\mathbf{r}_{mm}|^p}{\partial \mathbf{x}_m^k(n)}\right]. \quad (31)
\end{aligned}$$

To obtain the mathematical expression of (31), we still need to derive the partial derivative of $|\mathbf{r}_{mm'}|^p$, which can be calculated as

$$\begin{aligned}
&\frac{\partial}{\partial \mathbf{x}_m^k(n)} \mathbf{1}^T|\mathbf{r}_{mm'}|^p \\
&= \mathbf{1}^T \frac{\partial}{\partial \mathbf{x}_m^k(n)}\left(\mathbf{r}_{mm'} \odot \mathbf{r}_{mm'}^*\right)^{\frac{p}{2}} \\
&= \mathbf{1}^T\left[\frac{p}{2}|\mathbf{r}_{mm'}|^{p-2} \odot \frac{\partial}{\partial \mathbf{x}_m^k(n)}\left(\mathbf{r}_{mm'} \odot \mathbf{r}_{mm'}^*\right)\right] \\
&= \mathbf{1}^T\left(p|\mathbf{r}_{mm'}|^{p-2} \odot \mathrm{Re}\left[\left(\frac{\partial}{\partial \mathbf{x}_m^k(n)}\mathbf{r}_{mm'}\right) \odot \mathbf{r}_{mm'}^*\right]\right) \quad (32)
\end{aligned}$$

where

$$\begin{aligned}
\frac{\partial}{\partial \mathbf{x}_m^k(n)}\mathbf{r}_{mm'} &= \frac{\partial}{\partial \mathbf{x}_m^k(n)} \sum_{k=1}^{K} \mathbf{F}^H\left[\left(\mathbf{F}\bar{\mathbf{s}}_m^k\right) \odot \left(\mathbf{F}\bar{\mathbf{s}}_{m'}^k\right)^*\right] \\
&= \mathbf{F}^H\left[\left(\mathbf{F}\frac{\partial \bar{\mathbf{s}}_m^k}{\partial \mathbf{x}_m^k(n)}\right) \odot \left(\mathbf{F}\bar{\mathbf{s}}_{m'}^k\right)^*\right]. \quad (33)
\end{aligned}$$

For the term within the second summation operation, we have

$$\begin{aligned}
&\frac{\partial}{\partial \mathbf{x}_m^k(n)} \frac{\|\mathbf{r}_{m'm}\|_p^2}{\|\mathbf{r}_{m'm'} \odot \mathbf{w}_{\mathrm{ML}}\|_p^2} \\
&= \frac{2}{p}\left(\frac{\mathbf{1}^T|\mathbf{r}_{m'm}|^p}{\mathbf{w}_{\mathrm{ML}}^T|\mathbf{r}_{m'm'}|^p}\right)^{\frac{2}{p}-1} \frac{\partial}{\partial \mathbf{x}_m^k(n)}\left(\frac{\mathbf{1}^T|\mathbf{r}_{m'm}|^p}{\mathbf{w}_{\mathrm{ML}}^T|\mathbf{r}_{m'm'}|^p}\right) \\
&= \frac{2}{p}\left(\frac{\mathbf{1}^T|\mathbf{r}_{m'm}|^p}{\mathbf{w}_{\mathrm{ML}}^T|\mathbf{r}_{m'm'}|^p}\right)^{\frac{2}{p}}\left(\frac{\mathbf{1}^T}{\mathbf{1}^T|\mathbf{r}_{m'm}|^p}\frac{\partial}{\partial \mathbf{x}_m^k(n)}|\mathbf{r}_{m'm}|^p\right) \quad (34)
\end{aligned}$$

in which

$$\begin{aligned}
&\frac{\partial}{\partial \mathbf{x}_m^k(n)}|\mathbf{r}_{m'm}|^p \\
&= \frac{p}{2}\left(\mathbf{r}_{m'm} \odot (\mathbf{r}_{m'm})^*\right)^{\frac{p}{2}-1} \odot \frac{\partial}{\partial \mathbf{x}_m^k(n)}\left(\mathbf{r}_{m'm} \odot (\mathbf{r}_{m'm})^*\right) \\
&= p|\mathbf{r}_{m'm}|^{p-2}\mathrm{Re}\left[\frac{\partial}{\partial \mathbf{x}_m^k(n)}\mathbf{r}_{m'm} \odot (\mathbf{r}_{m'm})^*\right] \quad (35)
\end{aligned}$$

and

$$\frac{\partial}{\partial \mathbf{x}_m^k(n)}\mathbf{r}_{m'm} = \mathbf{F}^H\left[\left(\mathbf{F}\bar{\mathbf{s}}_{m'}^k\right) \odot \left(\mathbf{F}\left(j\bar{\mathbf{s}}_m^k \odot \bar{\mathbf{g}}_n\right)\right)^*\right]. \quad (36)$$

Substituting (32) and (33) into (31), substituting (35) and (36) into (34), we can obtain the partial derivative of $f_2(\mathbf{X})$ after some manipulations and stacking operator. The final partial derivative of the function component $f_2(\mathbf{X})$ is formally given as (37) shown at the bottom of this page.

C. Calculation of the Partial Derivative $\frac{\partial}{\partial \mathbf{x}_m^k} f_3(\mathbf{X})$

The function component $f_3(\mathbf{X})$ involves the summation of M different terms, the partial derivative of which can be expressed as

$$\begin{aligned}
\frac{\partial}{\partial \mathbf{x}_m^k(n)} \frac{\|\mathbf{r}_{mm}^J\|_p^2}{\|\mathbf{r}_{mm} \odot \mathbf{w}_{\mathrm{ML}}\|_p^2} &= \frac{2}{p}\left(\frac{\mathbf{1}^T|\mathbf{r}_{mm}^J|^p}{\mathbf{w}_{\mathrm{ML}}^T|\mathbf{r}_{mm}|^p}\right)^{\frac{2}{p}} \\
&\times \left(\frac{\mathbf{1}^T}{\mathbf{1}^T|\mathbf{r}_{mm}^J|^p}\frac{\partial|\mathbf{r}_{mm}^J|^p}{\partial \mathbf{x}_m^k(n)} - \frac{\mathbf{w}_{\mathrm{ML}}^T}{\mathbf{w}_{\mathrm{ML}}^T|\mathbf{r}_{mm}|^p}\frac{\partial|\mathbf{r}_{mm}|^p}{\partial \mathbf{x}_m^k(n)}\right). \quad (38)
\end{aligned}$$

Since we already obtained the partial derivative of $|\mathbf{r}_{mm}|^p$ in (24), we only need to find the expression of $|\mathbf{r}_{mm}^J|^p$. Applying the product rule to (9), we have

$$\frac{\partial|\mathbf{r}_{mm}^J|^p}{\partial \mathbf{x}_m^k(n)} = p|\mathbf{r}_{mm}^J|^{p-2}\mathrm{Re}\left(\frac{\partial}{\partial \mathbf{x}_m^k(n)}\mathbf{r}_{mm}^J \odot \left(\mathbf{r}_{mm}^J\right)^*\right). \quad (39)$$

Further, the partial derivative of $\mathbf{r}_{mm}^J$ can be calculated as

$$\frac{\partial}{\partial \mathbf{x}_m^k(n)}\mathbf{r}_{mm}^J = \frac{\partial}{\partial \mathbf{x}_m^k(n)}\mathbf{F}^H\left[\left(\mathbf{F}\bar{\mathbf{s}}_m^k\right) \odot \left(\mathbf{F}\bar{\xi}_m^k\right)^*\right]$$

$$\begin{aligned}
&\frac{\partial}{\partial \mathbf{x}_m^k} f_2(\mathbf{X}) \\
&= \sum_{m'=1}^{M}\left\{\left(\frac{\mathbf{1}^T|\mathbf{r}_{mm'}|^p}{\mathbf{w}_{\mathrm{ML}}^T|\mathbf{r}_{mm}|^p}\right)^{\frac{2}{p}}\left(\frac{2\bar{\mathbf{G}}^T}{\mathbf{1}^T|\mathbf{r}_{mm'}|^p}\mathrm{Im}\left[\left(\bar{\mathbf{s}}_m^k\right)^* \odot \left(\mathbf{F}^H\left[\mathbf{F}\left(|\mathbf{r}_{mm'}|^{p-2} \odot \mathbf{r}_{mm'}\right) \odot \left(\mathbf{F}\bar{\mathbf{s}}_{m'}^k\right)\right]\right)\right]\right.\right. \\
&\quad - \frac{4\bar{\mathbf{G}}^T}{\mathbf{w}_{\mathrm{ML}}^T|\mathbf{r}_{mm}|^p}\mathrm{Im}\left[\left(\bar{\mathbf{s}}_m^k\right)^* \odot \left(\mathbf{F}^H\left[\mathbf{F}\left(\mathbf{w}_{\mathrm{ML}} \odot |\mathbf{r}_{mm}|^{p-2} \odot \mathbf{r}_{mm}\right) \odot \left(\mathbf{F}\bar{\mathbf{s}}_m^k\right)\right]\right)\right]\Big) \\
&\quad \left.\left. + \frac{2\bar{\mathbf{G}}^T}{\mathbf{1}^T|\mathbf{r}_{m'm}|^p}\mathrm{Im}\left[\left(\left(\bar{\mathbf{s}}_m^k\right)^* \odot \left(\mathbf{F}^H\left(\left[\mathbf{F}\left(|\mathbf{r}_{m'm}|^{p-2} \odot (\mathbf{r}_{m'm})\right)\right]^* \odot \left(\mathbf{F}\bar{\mathbf{s}}_{m'}^k\right)\right)\right)\right)\right]\right\}. \quad (37)
\end{aligned}$$

$$\frac{\partial}{\partial \mathbf{x}_m^k(n)} f_3(\mathbf{X}) = \left(\frac{\mathbf{1}^T \left|\mathbf{r}_{mm}^J\right|^p}{\mathbf{w}_{\mathrm{ML}}^T |\mathbf{r}_{mm}|^p}\right)^{\frac{2}{p}} \left\{ \frac{2\bar{\mathbf{G}}^T}{\mathbf{1}^T \left|\mathbf{r}_{mm}^J\right|^p} \left[\mathrm{Im}\left(\left(\bar{\mathbf{s}}_m^k\right)^* \odot \left[\mathbf{F}^H \left(\left[\mathbf{F}\left(\mathbf{r}_{mm}^J \odot \left|\mathbf{r}_{mm}^J\right|^{p-2} \right) \right] \odot \left(\mathbf{F}\bar{\xi}_m^k\right) \right) \right] \right) \right.\right.$$
$$+\mathrm{Im}\left(\left(\bar{\mathbf{J}}\,\mathrm{diag}\left(\bar{\mathbf{s}}_m^k\right)\right)^H \left[\mathbf{F}^H \left(\left[\mathbf{F}\left(\mathbf{r}_{mm}^J \odot \left|\mathbf{r}_{mm}^J\right|^{p-2} \right) \right]^* \odot \left(\mathbf{F}\bar{\mathbf{s}}_m^k\right) \right) \right] \right) \Big]$$
$$\left. -\frac{4}{\mathbf{w}_{\mathrm{ML}}^T |\mathbf{r}_{mm}|^p} \bar{\mathbf{G}}^T \mathrm{Im}\left[\left(\bar{\mathbf{s}}_m^k\right)^* \odot \left(\mathbf{F}^H \left(\mathbf{F}\left(\mathbf{r}_{mm} \odot |\mathbf{r}_{mm}|^{p-2} \odot \mathbf{w}_{\mathrm{ML}} \right) \odot \left(\mathbf{F}\bar{\mathbf{s}}_m^k\right) \right) \right) \right] \right\}. \tag{42}$$

$$\frac{\partial}{\partial \mathbf{x}_m^k} f_4(\mathbf{X})$$
$$= \sum_{m'=1}^{M} \left(\frac{\mathbf{1}^T \left|\mathbf{r}_{mm'}^J\right|^p}{\mathbf{w}_{\mathrm{ML}}^T |\mathbf{r}_{mm}|^p}\right)^{\frac{2}{p}} \left\{ \frac{2\bar{\mathbf{G}}^T}{\mathbf{1}^T \left|\mathbf{r}_{mm'}^J\right|^p} \mathrm{Im}\left(\left[\left(\bar{\mathbf{s}}_m^k\right)^* \odot \left(\mathbf{F}^H \left(\mathbf{F}\left(\mathbf{r}_{mm'}^J \odot \left|\mathbf{r}_{mm'}^J\right|^{p-2} \right) \odot \left(\mathbf{F}\bar{\xi}_{m'}^k\right) \right) \right) \right] \right) \right.$$
$$\left. -\frac{4\bar{\mathbf{G}}^T}{\mathbf{w}_{\mathrm{ML}}^T |\mathbf{r}_{mm}|^p} \mathrm{Im}\left[\left(\bar{\mathbf{s}}_m^k\right)^* \odot \left(\mathbf{F}^H \left(\mathbf{F}\left(\mathbf{r}_{mm} \odot |\mathbf{r}_{mm}|^{p-2} \odot \mathbf{w}_{\mathrm{ML}} \right) \odot \left(\mathbf{F}\bar{\mathbf{s}}_m^k\right) \right) \right) \right] \right\}$$
$$+ \sum_{m'=1}^{M} \left(\frac{\mathbf{1}^T \left|\mathbf{r}_{m'm}^J\right|^p}{\mathbf{w}_{\mathrm{ML}}^T |\mathbf{r}_{m'm'}|^p}\right)^{\frac{2}{p}} \left(\frac{2\bar{\mathbf{G}}^T}{\mathbf{1}^T \left|\mathbf{r}_{m'm}^J\right|^p} \mathrm{Im}\left[\left(\bar{\mathbf{J}}\,\mathrm{diag}\left(\bar{\mathbf{s}}_m^k\right)\right)^H \left(\mathbf{F}^H \left(\left[\mathbf{F}\left(\left|\mathbf{r}_{m'm}^J\right|^{p-2} \odot \left(\mathbf{r}_{m'm}^J\right) \right) \right]^* \odot \left(\mathbf{F}\bar{\mathbf{s}}_{m'}^k\right) \right) \right) \right] \right) \tag{47}$$

$$= \mathbf{F}^H \left[\left(\mathbf{F}\frac{\partial \bar{\mathbf{s}}_m^k}{\partial \mathbf{x}_m^k(n)} \right) \odot \left(\mathbf{F}\bar{\xi}_m^k\right)^* + \left(\mathbf{F}\bar{\mathbf{s}}_m^k\right) \odot \left(\mathbf{F}\frac{\partial \bar{\xi}_m^k}{\partial \mathbf{x}_m^k(n)} \right)^* \right] \tag{40}$$

in which

$$\frac{\partial \bar{\xi}_m^k}{\partial \mathbf{x}_m^k(n)} = j\bar{\mathbf{J}}\,\mathrm{diag}\left(\bar{\mathbf{s}}_m^k\right) \bar{\mathbf{g}} \tag{41}$$

where $\bar{\mathbf{J}}$ denotes a $(2L-1)\times(2L-1)$-dimensional matrix, with the $L \times L$ submatrix in the top-left corner determined by $\mathbf{J}$. Combing the equations (24), (39)–(41), the final partial derivative of function component $f_3(\mathbf{X})$ can be easily obtained, as given in (42) shown at the top of this page.

D. Calculation of the Partial Derivative $\frac{\partial}{\partial \mathbf{x}_m^k} f_4(\mathbf{X})$

The function component $f_4(\mathbf{X})$ involves two nested summations over the channel dimensions. To compute its partial derivative, we first decouple the derivative into two independent summation terms, resulting in the following expression:

$$\frac{\partial}{\partial \mathbf{x}_m^k(n)} f_4(\mathbf{X}) = \sum_{m'=1}^{M} \frac{\partial}{\partial \mathbf{x}_m^k(n)} \frac{\left\|\mathbf{r}_{mm'}^J\right\|_p^2}{\left\|\mathbf{r}_{mm} \odot \mathbf{w}_{\mathrm{ML}}\right\|_p^2} + \sum_{m'=1}^{M} \frac{\partial}{\partial \mathbf{x}_m^k(n)} \frac{\left\|\mathbf{r}_{m'm}^J\right\|_p^2}{\left\|\mathbf{r}_{m'm'} \odot \mathbf{w}_{\mathrm{ML}}\right\|_p^2}. \tag{43}$$

For each term within the first summation operation, we have

$$\frac{\partial}{\partial \mathbf{x}_m^k(n)} \frac{\left\|\mathbf{r}_{mm'}^J\right\|_p^2}{\left\|\mathbf{r}_{mm} \odot \mathbf{w}_{\mathrm{ML}}\right\|_p^2} = \frac{2}{p} \left(\frac{\mathbf{1}^T \left|\mathbf{r}_{mm'}^J\right|^p}{\mathbf{w}_{\mathrm{ML}}^T |\mathbf{r}_{mm}|^p}\right)^{\frac{2}{p}} \times \left(\frac{\mathbf{1}^T}{\mathbf{1}^T \left|\mathbf{r}_{mm'}^J\right|^p} \frac{\partial \left|\mathbf{r}_{mm'}^J\right|^p}{\partial \mathbf{x}_m^k(n)} - \frac{\mathbf{w}_{\mathrm{ML}}^T}{\mathbf{w}_{\mathrm{ML}}^T |\mathbf{r}_{mm}|^p} \frac{\partial |\mathbf{r}_{mm}|^p}{\partial \mathbf{x}_m^k(n)} \right) \tag{44}$$

where

$$\frac{\partial \left|\mathbf{r}_{mm'}^J\right|^p}{\partial \mathbf{x}_m^k(n)} = p\left|\mathbf{r}_{mm'}^J\right|^{p-2} \odot \mathrm{Re}\left(\frac{\partial \mathbf{r}_{mm'}^J}{\partial \mathbf{x}_m^k(n)} \odot \left(\mathbf{r}_{mm'}^J\right)^* \right) \tag{45}$$

and

$$\frac{\partial \mathbf{r}_{mm'}^J}{\partial \mathbf{x}_m^k(n)} = j\mathbf{F}^H \left[\left(\mathbf{F}\left(\bar{\mathbf{s}}_m^k \odot \bar{\mathbf{g}}_n \right) \right) \odot \left(\mathbf{F}\bar{\xi}_{m'}^k\right)^* \right]. \tag{46}$$

Leveraging equations (24), (44)–(46), the partial derivative of the first term in (43) can be obtained, and the partial derivative of the second term can be obtained similarly. Consequently, the final partial derivative of function component $f_4(\mathbf{X})$ can be expressed as (47) shown at the top of this page. With (29), (37), (42), and (47) at hand, the gradient of the objective function with respect to $\mathbf{X}$ can be obtained, and the proposed Algorithm 2 can proceed.

REFERENCES

[1] P. Heidenreich, A. Zoubir, I. Bilik, M. Greco, and M. Torlak, "Editorial: Introduction to the issue on recent advances in automotive radar signal processing," *IEEE J. Sel. Topics Signal Process.*, vol. 15, no. 4, pp. 861–864, Jun. 2021.

[2] B. Xue, G. Zhang, F. Gini, M. S. Greco, and H. Leung, "A high-order motion parameter estimation of moving target for miniature Dechirped MMW radar," *IEEE Trans. Aerosp. Electron. Syst.*, vol. 60, no. 6, pp. 8332–8348, Dec. 2024.

[3] A. Tang, S. Li, and X. Wang, "Self-interference-resistant IEEE 802.11ad-based joint communication and automotive radar design," *IEEE J. Sel. Topics Signal Process.*, vol. 15, no. 6, pp. 1484–1499, Nov. 2021.

[4] Y. Liu, H. Gao, M. S. Greco, and F. Gini, "Robust DOA estimation of incoherently distributed sources considering mixed circular and noncircular signals in impulsive noise," *IEEE Signal Process. Lett.*, vol. 31, pp. 1900–1904, 2024.

[5] S. Jin and S. Roy, "FMCW radar network: Multiple access and interference mitigation," *IEEE J. Sel. Topics Signal Process.*, vol. 15, no. 4, pp. 968–979, Jun. 2021.

[6] X. Qiu, W. Jiang, Y. Liu, S. Chatzinotas, F. Gini, and M. S. Greco, "Learning-enhanced Riemannian gradient descent method for transmit-receive joint design towards ISRJ suppression," *IEEE Trans. Aerosp. Electron. Syst.*, to be published, doi: 10.1109/TAES.2024.3525455.

[7] P. Stinco, M. Greco, F. Gini, and B. Himed, "Cognitive radars in spectrally dense environments," *IEEE Aerosp. Electron. Syst. Mag.*, vol. 31, no. 10, pp. 20–27, Oct. 2016.

[8] X. Zhang, W. Jiang, X. Qiu, and Y. Liu, "Worst-case Riemannian optimization with uncertain target steering vector for slow-time transmit sequence of cognitive radar," *IEEE Trans. Aerosp. Electron. Syst.*, vol. 61, no. 2, pp. 4030–4044, Apr. 2025.

[9] C. G. Tsinos, A. Arora, S. Chatzinotas, and B. Ottersten, "Joint transmit waveform and receive filter design for dual-function radar-communication systems," *IEEE J. Sel. Topics Signal Process.*, vol. 15, no. 6, pp. 1378–1392, Nov. 2021.

[10] X. Qiu, W. Jiang, Y. Liu, S. Chatzinotas, F. Gini, and M. S. Greco, "Constrained Riemannian manifold optimization for the simultaneous shaping of ambiguity function and transmit beampattern," *IEEE Trans. Aerosp. Electron. Syst.*, to be published, doi: 10.1109/TAES.2024.3520951.

[11] B. Xue, G. Zhang, Q. Dai, Z. Fang, and H. Leung, "Waveform diversity design of OFDM chirp for miniature millimeter-wave MIMO radar based on dechirp," *IEEE Trans. Geosci. Remote Sens.*, vol. 61, 2023, Art. no. 5107616.

[12] M. Wang, X. Li, L. Gao, Z. Sun, G. Cui, and T. S. Yeo, "Signal accumulation method for high-speed maneuvering target detection using airborne coherent MIMO radar," *IEEE Trans. Signal Process.*, vol. 71, pp. 2336–2351, 2023.

[13] D. An et al., "Per-user dynamic controllable waveform design for dual function radar-communication system," *IEEE Trans. Aerosp. Electron. Syst.*, vol. 61, no. 2, pp. 3346–3360, Apr. 2025.

[14] D. Zhou, M. Yang, H. Lian, T. Ma, M. S. Greco, and F. Gini, "Moving target detection with SNR diversity for distributed coherent aperture radar on moving platforms," *IEEE Trans. Veh. Technol.*, to be published, doi: 10.1109/TVT.2024.3505615.

[15] S. Wei, Y. Fang, Y. Song, S. Wei, and L. Zhang, "Joint jam perception and adaptive waveform optimization for anti-interrupted sampling repeater jamming," *IEEE Trans. Aerosp. Electron. Syst.*, vol. 60, no. 1, pp. 1129–1147, Feb. 2024.

[16] V. P. Riabukha, A. V. Semeniaka, Y. A. Katiushyn, and D. V. Atamanskiy, "Pulse DRFM jamming formation and its mathematical simulation," in *Proc. IEEE 2nd Ukrainian Microw. Week*, 2022, pp. 654–659.

[17] M. J. Sparrow and J. Cikalo, "ECM techniques to counter pulse compression radar," US Patent 7,081,846, Jul. 25, 2006.

[18] S. B. S. Hanbali, "Countering self-protection smeared spectrum jamming against chirp radars," *IET Radar, Sonar Navigation*, vol. 15, no. 4, pp. 382–389, 2021.

[19] Y. Zhang and K. Ding, "Research on SMSP jamming suppression based on matched filtering in FRFT domain," in *Proc. 7th Int. Conf. Comput. Inf. Sci. Appl. Technol.*, 2024, pp. 963–966.

[20] Y. Zhao, C. Shang, Z. Han, N. Han, and H. Xie, "Fractional Fourier transform and compressed sensing adaptive countering smeared spectrum jamming," *J. Electron. Inf. Technol.*, vol. 41, no. 5, pp. 1047–1054, 2019.

[21] C. Wu, B. Chen, M. Yang, and M. Dong, "A study on parameter estimation and suppression for smeared spectrum jamming based on short-time Fourier transform," *EURASIP J. Wireless Commun. Netw.*, vol. 2020, pp. 1–16, 2020.

[22] X. Wang et al., "SMSP interference suppression method based on time-domain interference matching," in *Proc. IET Int. Radar Conf.*, 2023, vol. 2023, pp. 991–997.

[23] X. Wang, H. Chen, W. Liu, B. Li, W. Shen, and M. Ni, "ECCM scheme against SMSP interference based on interference reconstruction," in *Proc. IEEE 6th Adv. Inf. Manage., Communicates, Electron. Automat. Control Conf.*, 2024, vol. 6, pp. 161–167.

[24] P. Wan, G. Liao, J. Xu, and X. Fu, "SMSP mainlobe jamming suppression with FDA-MIMO radar based on FASTICA algorithm," *Sensors*, vol. 23, no. 12, 2023, Art. no. 5619.

[25] M. Wang et al., "Multi-channel signal integration approach for high-speed target detection in coherent MIMO radar system," *IEEE Trans. Aerosp. Electron. Syst.*, vol. 60, no. 6, pp. 8298–8315, Dec. 2024.

[26] S. Lu, G. Cui, W. Yi, L. Kong, and X. Yang, "Radar waveform design against signal-dependent jamming," in *Proc. 2017 IEEE Radar Conf.*, 2017, pp. 1075–1080.

[27] S. Lu, G. Cui, X. Yu, L. Kong, and X. Yang, "Cognitive radar waveform design against signal-dependent modulated jamming," *Prog. Electromagnetics Res. B*, vol. 80, pp. 59–77, 2018.

[28] X. Qiu, C. Yang, W. Jiang, and Y. Liu, "Joint design of transmit waveform and receive filter for cross ambiguity function synthesis," *IEEE Wireless Commun. Lett.*, vol. 13, no. 3, pp. 839–843, Mar. 2024.

[29] T. Jiang et al., "Dictionary learning and waveform design for dense false target jamming suppression," *Appl. Comput. Electromagnetics Soc. J.*, vol. 36, pp. 1173–1181, 2021.

[30] L. Zuo, Z. Lan, X. Lu, Y. Gao, and L. Mao, "Joint transmit-receive filter design with lower APSL and ICPL to suppress interference," *IEEE Trans. Aerosp. Electron. Syst.*, vol. 60, no. 3, pp. 3673–3687, Jun. 2024.

[31] S. D. Blunt, M. Cook, J. Jakabosky, J. De Graaf, and E. Perrins, "Polyphase-coded FM (PCFM) radar waveforms, Part I: Implementation," *IEEE Trans. Aerosp. Electron. Syst.*, vol. 50, no. 3, pp. 2218–2229, Jul. 2014.

[32] C.-E. Sundberg, "Continuous phase modulation," *IEEE Commun. Mag.*, vol. 24, no. 4, pp. 25–38, Apr. 1986.

[33] S. D. Blunt, J. Jakabosky, M. Cook, J. Stiles, S. Seguin, and E. Mokole, "Polyphase-coded FM (PCFM) radar waveforms, Part II: Optimization," *IEEE Trans. Aerosp. Electron. Syst.*, vol. 50, no. 3, pp. 2230–2241, Jul. 2014.

[34] L. Ryan, J. Jakabosky, S. D. Blunt, C. Allen, and L. Cohen, "Optimizing polyphase-coded FM waveforms within a LINC transmit architecture," in *Proc. IEEE Radar Conf.*, 2014, pp. 835–839.

[35] J. Jakabosky, P. McCormick, and S. D. Blunt, "Implementation and design of physical radar waveform diversity," *IEEE Aerosp. Electron. Syst. Mag.*, vol. 31, no. 12, pp. 26–33, Dec. 2016.

[36] C. A. Mohr, P. M. McCormick, C. A. Topliff, S. D. Blunt, and J. M. Baden, "Gradient-based optimization of PCFM radar waveforms," *IEEE Trans. Aerosp. Electron. Syst.*, vol. 57, no. 2, pp. 935–956, Apr. 2021.

[37] C. A. Mohr, P. M. McCormick, and S. D. Blunt, "Optimized complementary waveform subsets within an FM noise radar CPI," in *Proc. IEEE Radar Conf.*, 2018, pp. 0687–0692.

[38] X. Qiu, W. Jiang, X. Zhang, M. S. Greco, and F. Gini, "Simultaneous design of PCFM waveforms and receive filters towards ISRJ suppression," *IEEE Geosci. Remote Sens. Lett.*, vol. 21, 2024, Art. no. 3509305.

[39] C. C. Jones, C. A. Mohr, P. M. McCormick, and S. D. Blunt, "Complementary frequency modulated radar waveforms and optimised receive processing," *IET Radar, Sonar Navigation*, vol. 15, no. 7, pp. 708–723, 2021.

[40] Y. Sun, H. Fan, J. Wang, L. Ren, E. Mao, and T. Long, "Optimization of diverse PCFM waveforms and joint mismatched filters," *IEEE Trans. Aerosp. Electron. Syst.*, vol. 57, no. 3, pp. 1840–1854, Jun. 2021.

[41] D. Zhao, Y. Wei, and Y. Liu, "PCFM radar waveform design with spectral and correlation considerations," *IEEE Trans. Aerosp. Electron. Syst.*, vol. 53, no. 6, pp. 2885–2898, Dec. 2017.

[42] D. Zhao and Y. Liu, "Over-sampled polyphase code design for physical implementation with spectral and correlation consideration," in *Proc. IEEE Radar Conf.*, 2016, pp. 1–6.

[43] C. A. Mohr, P. M. McCormick, S. D. Blunt, and C. Mott, "Spectrally-efficient FM noise radar waveforms optimized in the logarithmic domain," in *Proc. IEEE Radar Conf.*, 2018, pp. 0839–0844.

[44] F. Wang, N. Li, C. Pang, Y. Li, and X. Wang, "Algorithm for designing PCFM waveforms for simultaneously polarimetric radars," *IEEE Trans. Geosci. Remote Sens.*, vol. 62, 2023, Art. no. 5100716.

[45] M. S. Greco, F. Gini, and P. Stinco, "Cognitive radars: Some applications," in *Proc. IEEE Glob. Conf. Signal Inf. Process.*, 2016, pp. 1077–1082.
[46] Y. Cao, H. Zhang, Y. Qin, H. Zhu, J. Cao, and N. Ma, "Joint denoising blind source separation algorithm for anti-jamming," in *Proc. 4th Int. Conf. Inf. Commun. Signal Process.*, 2021, pp. 27–35.
[47] W. Luo, R. Yang, H. Jin, X. Li, H. Li, and K. Liang, "Single channel blind source separation of complex signals based on spatial-temporal fusion deep learning," *IET Radar, Sonar Navigation*, vol. 17, no. 2, pp. 200–211, 2023.
[48] M. Fornasier and H. Rauhut, "Iterative thresholding algorithms," *Appl. Comput. Harmon. Anal.*, vol. 25, no. 2, pp. 187–208, 2008.
[49] J. Jakabosky, S. D. Blunt, and B. Himed, "Optimization of "overcoded" radar waveforms," in *Proc. IEEE Radar Conf.*, 2014, pp. 1460–1465.
[50] Y. Tan, H. An, Z. Li, J. Wu, H. Yang, and J. Yang, "Complementary waveform design for SAR range sidelobe suppression," *IEEE Trans. Geosci. Remote Sens.*, vol. 63, 2025, Art. no. 5205011.
[51] X. Qiu, W. Jiang, X. Zhang, and K. Huo, "Quartic Riemannian trust region algorithm for cognitive radar ambiguity function shaping," *IEEE Geosci. Remote Sens. Lett.*, vol. 19, 2022, Art. no. 4022005.
[52] M. J. Kochenderfer and T. A. Wheeler, *Algorithms for Optimization*. Cambridge, MA, USA: MIT Press, 2019.
[53] C. Cheng, Y. Wu, Q. Liu, F. Hua, Y. Zhang, and X. He, "Fast high-dimensional parameter optimization for turbine blade manufacturing using the powerball L-BFGS method under incomplete measurements," *IEEE Trans. Instrum. Meas.*, vol. 73, 2024, Art. no. 3524912.
[54] S. Boyd and L. Vandenberghe, *Convex Optimization*. Cambridge, U.K.: Cambridge Univ. Press, 2004.
[55] H. Kai et al., "A recognition method of aerospace time-sensitive targets based on radar high resolution range profile," *Aero Weaponry*, vol. 29, no. 2, pp. 13–18, 2022.

Xiangfeng Qiu (Graduate Student Member, IEEE) was born in 1997. He received the B.S. degree in information engineering from Hainan University, Haikou, China, in 2019, and the M.S. degree in information engineering degree, in 2021, from the National University of Defense Technology, Changsha, China, where he is currently working toward the Ph.D. degree in information and communication engineering.

From 2016 to 2018, he attended a joint training program with Tianjin University, Tianjin, China. He is currently a visiting Ph.D. student with the University of Pisa, Pisa, Italy. His research interests include numerical optimization and radar waveform design.

Weidong Jiang was born in 1968. He received the B.S., M.S., and Ph.D. degrees in information engineering from the National University of Defense Technology (NUDT), Changsha, China, in 1991, 1997, and 2001, respectively.

He is currently a Research Fellow with the College of Electronic Science and Technology, NUDT. His research interests include target recognition and radar signal processing.

Xinyu Zhang received the B.S. and Ph.D. degrees in information engineering from the Beijing Institute of Technology, Beijing, China, in 2011 and 2017, respectively.

From 2015 to 2017, he visited Ohio State University, Columbus, OH, USA, as a Visiting Scholar. In 2017, he joined the National University of Defense Technology (NUDT), Changsha, China, as a Post-doctor, where he is currently an Associate Professor. His research interests include array signal processing, auto-target detection, and waveform optimization.

Yongxiang Liu received the B.S. and Ph.D. degrees in information and communication engineering from the College of Electronic Science, National University of Defense Technology, Changsha, China, in 1997 and 2004, respectively.

He is currently a Full Professor with the National University of Defense Technology. His research interests include radar imaging, SAR image interpretation, and artificial intelligence.

Symeon Chatzinotas (Fellow, IEEE) received the M.Eng. degree in telecommunications from the Aristotle University of Thessaloniki, Thessaloniki, Greece, and the M.Sc. and Ph.D. degrees in electronic engineering from University of Surrey, Guildford, U.K., in 2003, 2006 and 2009 respectively.

He was an Visiting Professor with the University of Parma, Parma, Italy, and contributed in numerous R&D projects for the Institute of Telematics and Informatics, Center of Research and Technology Hellas and Mobile Communications Research Group, Center of Communication Systems Research, University of Surrey. He is currently a Full Professor/Chief Scientist I and Head of the research group SIGCOM, Interdisciplinary Centre for Security, Reliability and Trust, University of Luxembourg, Esch-sur-Alzette, Luxembourg. In parallel, he is an Adjunct Professor with the Department of Electronic Systems, Norwegian University of Science and Technology, Trondheim, Norway, and a Collaborating Scholar with the Institute of Informatics & Telecommunications, National Center for Scientific Research "Demokritos," Agia Paraskevi, Greece. He has authored more than 800 technical papers in refereed international journals, conferences, and scientific books.

Dr. Chatzinotas was the recipient of numerous awards and recognitions, including the IEEE Fellowship and an IEEE Distinguished Contributions Award. He is currently in the editorial board of IEEE TRANSACTIONS ON COMMUNICATIONS, IEEE OPEN JOURNAL OF VEHICULAR TECHNOLOGY, and the *International Journal of Satellite Communications and Networking*.

Maria Sabrina Greco (Fellow, IEEE) received the graduate degree in electronic engineering and the Ph.D. degree in telecommunication engineering from the University of Pisa, Pisa, Italy, in 1993 and 1998, respectively.

From 1997 to 1998, she was with Georgia Tech Research Institute, Atlanta, GA, USA, as a Visiting Research Scholar. In 1993, she joined the Department of Information Engineering, University of Pisa, where, since 2017, she has been a Full Professor. From 2015 to 2015 and from 2018 to 2018, she visited as an Invited Professor with Universitá Paris-Sud, CentraleSupélec, Paris, France. She has coauthored many book chapters and about 200 journal articles and conference papers. Her research interests include statistical signal processing, estimation, and detection theory, in particular, clutter models, coherent and incoherent detection in non-Gaussian clutter, CFAR techniques, radar waveform diversity, bistatic or multistatic active and passive radars, and cognitive radars.

Dr. Greco was the co-recipient of the 2001 and 2012 IEEE Aerospace and Electronic Systems Society's Barry Carlton Awards for Best Paper and the 2019 *EURASIP Journal on Advances in Signal Processing* Best Paper Award and a recipient of the 2008 Fred Nathanson Young Engineer of the Year Award for contributions to signal processing, estimation, and detection theory, and the IEEE Aerospace and Electronic Systems Society (AESS) Board of Governors Exceptional Service Award for Exemplary Service and Dedication and Professionalism, as the Editor-in-Chief of *IEEE Aerospace and Electronic Systems Magazine*. She was the Guest Editor for a few special issues. She is an Associate Editor for *IET Proceedings-Radar, Sonar and Navigation* and *IET Signal Processing*, and the Editor-in-Chief of Springer *Journal of Advances in Signal Processing*. She was the Chair of the IEEE AESS Radar Panel from 2015 to 2016. She was the general chair, the technical program chair, and an organizing committee member for many international conferences for more than ten years. She is a member of the IEEE AESS Board of Governors (BoG) and the IEEE Signal Processing Society (SPS) BoG from 2015 to 2017. She was the SPS Distinguished Lecturer from 2014 to 2015, the AESS Distinguished Lecturer from 2015 to 2020, and the AESS VP Publications from 2018 to 2020. She is currently the IEEE SPS Director-at-Large for Region 8.

Fulvio Gini (Fellow, IEEE) received the doctor of engineering (cum laude) and research doctorate in electronic engineering from the University of Pisa, Pisa, Italy, in 1990 and 1995, respectively.

In 1993, he joined the Department of Information Engineering at the University of Pisa, Pisa, Italy, where he has been a Full Professor since 2006, and has served as the Deputy Head of the Department since 2016. He has authored or coauthored 13 book chapters, 184 journal papers, 195 conference papers, and holds 2 national patents.

Dr. Gini was the recipient of multiple awards, including the IEEE Aerospace and Electronic Systems Society's (AESS) Barry Carlton Award for Best Paper in 2001 and 2012, the 2020 *EURASIP Journal on Advances in Signal Processing* Best Paper Award, the 2022 IEEE AESS Warren White Award for Excellence in Radar Engineering, the 2020 EURASIP Meritorious Service Award, the 2003 IEE Achievement Award, and the 2003 IEEE AESS Nathanson Award. He is an Associate Editor for IEEE TRANSACTIONS ON AEROSPACE AND ELECTRONIC SYSTEMS (AES) from 2007 to present, and the Elsevier *Signal Processing* journal from 2006 to present. In addition, he serves as the Specialty Chief Editor for the "Radar Signal Processing" section of the journal *Frontiers in Signal Processing* from 2021 to present. He is the IEEE AESS Awards Chair and was a member of the IEEE AESS Board of Governors (BoG) from 2017 to 2022, and 2025 to 2027, and the IEEE Signal Processing Society BoG from 2021 to 2023. He also served as the EURASIP President from 2013 to 2016 and was the General Co-Chair of International Conference on Acoustics, Speech, and Signal Processing 2014. His H-index is 56, with 11 590 citations (source: Google Scholar).